Computer Modeling of ICF Target Chamber Phenomena

G.A. Moses and R.R. Peterson

January 1993
(revised June 1993)

UWFDM-909

Submitted to Lasers and Particle Beams.

FUSION TECHNOLOGY INSTITUTE

UNIVERSITY OF WISCONSIN

MADISON WISCONSIN

Computer Modeling of

ICF Target Chamber Phenomena

Gregory A. Moses and Robert R. Peterson

Fusion Technology Institute

University of Wisconsin-Madison

1500 Johnson Drive

Madison, WI, 53706 USA

January 1993

UWFDM-909

Submitted to Lasers and Particle Beams

Abstract

The target chamber of an ICF power plant or high yield test facility must be designed to absorb the target produced x rays and ions and survive the resulting effects. The target chamber conditions must be restored in fractions of a second for high repetition rate power applications. Computer modeling of these phenomena is essential because equivalent conditions cannot be produced in laboratory experiments prior to the first ignition of high yield ICF targets. Choices of models are dictated by specific reactor design strategies. The two major strategies, gas protection and sacrificial first surfaces, are used as a guide to our discussion. Physical models for ion, electron, and x-ray deposition are discussed, along with physical and numerical modeling of the resulting phase changes in target chamber structures. The hydrodynamics and radiative transfer in the target chamber vapors and plasmas is a central topic of this paper.

1. Introduction

Generation of one thousand megawatts (1000 MW) of net electric power from inertial confinement fusion (ICF) requires that high gain microexplosions occur several times per second and that the energy released from the fusion reactions is about one hundred times greater than the driver energy required to implode and ignite the fuel (Hogan 1992). Containment of the microexplosions and recovery of the fusion energy are two major challenges of ICF reactor design. The microexplosion creates a rapidly expanding, very high energy density, high Z plasma. High gain microexplosions have yet to be demonstrated in the laboratory and similar plasma conditions are difficult to achieve by any other means. For these reasons, designs of conceptual reactor chambers to contain the microexplosion and recover the fusion energy are based almost exclusively upon the results of numerical models of the relevant phenomena. These phenomena, their modeling, and the codes that are commonly used are the subject of this paper.

The numerical modeling of ICF reactor chamber phenomena follows from the specific details of any particular design. To date, nearly 50 different conceptual reactor designs have been completed (Meier 1992; Waganer 1992; Crandall 1992). A major element in all reactor designs is a mechanism to protect the plasma-facing surface (or "first surface") from the x rays and expanding ionic debris from the microexplosion. This radiation represents a severe transient heat flux on this first surface. Without some active form of protection, a steel reactor chamber would require a 20-30 meter diameter to avoid ablation of the plasma-facing surface on each ICF shot. The two most common first surface protection schemes, gas protection and sacrificial first surface, will guide this discussion in Sections 2 and 3. The design strategy and phenomenology associated with these approaches will serve as a prologue to the discussion of modeling and numerics in Section 4. Section 5 is a discussion of new developments in reactor chamber modeling that are not yet in common use.

2. Gas Protection

2.1. Design Strategy

The idea of gas protection is to introduce a low pressure inert gas into the target chamber to absorb the short range x rays and slow down and stop the ionic debris before they reach the first surface. This heats the gas to plasma conditions. This plasma must reradiate its energy to the first surface over a much longer time scale than the original microexplosion to reduce the instantaneous heat flux and protect the first surface from ablation. Following reradiation the gas must be pumped from the chamber for further energy recovery and re-establishment of chamber conditions for the next shot.

The type of gas and the pressure of the gas in the reactor chamber are constrained by several factors. The most important of these is beam propagation. This sets different constraints for laser, heavy ion, and light ion beams. The first surface radius must be large enough that the harmful x rays and ions are stopped or attenuated to a sufficient degree in the gas so that those reaching the first surface do not structurally damage it. Finally, the gas pressure and chamber volume must be matched so that conditions are re-established in the time between shots. This requires active pumping of the chamber and replenishment of the gas. For near term, single shot experiments, this constraint is not important.

A number of recent reactor designs have used the gas protection scheme (Olson 1987; Sviatoslavsky 1990; Meier 1992; Peterson 1992; Sviatoslavsky 1991; Sviatoslavsky 1992; Sviatoslavsky 1992a). The SIRIUS-T direct drive laser fusion reactor chamber, containment building, and final focusing mirrors are shown in Figure 1. The 4 meter radius cavity is filled with 1 torr of xenon gas and the plasma-facing surface is a 4-D carbon composite. The target yield is 100 MJ with a KrF laser energy of 2 MJ and the chamber is fired 10 times per second. The plasma-facing surface is estimated to reach a maximum temperature of 1500 K following each microexplosion.

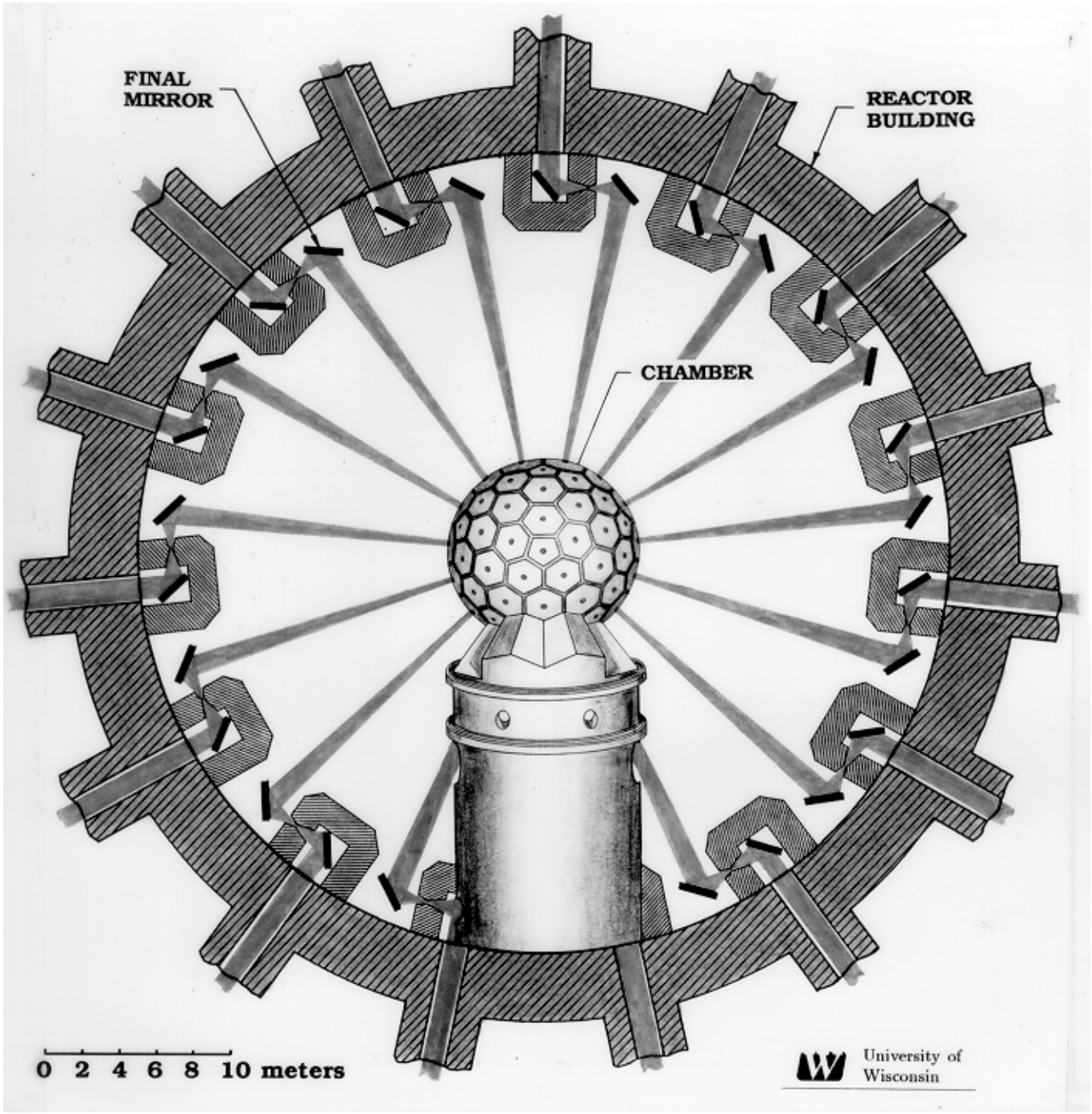

Figure 1. SIRIUS-T direct drive laser fusion reactor chamber, containment building and final focusing mirrors.

2.2. Phenomenology

Design points for first surface radius, gas pressure, etc. in conceptual reactor designs are chosen through tradeoff studies aimed at satisfying all physical constraints. The physical phenomenology of beam propagation in a gas, x ray and ion attenuation, plasma reradiation, first surface thermo-mechanical response, shock wave propagation and cavity clearing must be understood to the degree necessary to model these phenomena.

2.2.1. Beam Propagation

Laser Beams. Intense laser beams break down and ionize gases by multiphoton absorption and electron cascade. This can occur at intensities of 10^{12} watts/cm^2. Lasers for reactor applications use high f-number optics to minimize the surface area of the final optical elements and to position them as far from the target as possible (10-100 meters). Intensities of 10^{15} watts/cm^2 at the target and the use of f-10 or f-20 optics implies that an intensity of 10^{12} watts/cm^2 is reached tens of centimeters from the target. Analytical estimates of beam refraction and laboratory experiments indicate that several torr of gas will not seriously degrade the laser beam characteristics at the target. However, exact reactor conditions must still be verified experimentally.

Heavy Ion Beams. Near relativistic heavy ions (10 GeV Bi) are "stiff" enough to electromagnetic forces that ballistic propagation over a distance of 5-10 meters in the absence of background charged particles is thought to be possible. The position of the final focusing magnet is determined by the emittance of the beam and the required spot size on the target. Propagation of heavy ion beams in a gas background is dominated by plasma effects associated with the additional charge carriers. This mode of transport has the obvious advantages of using the gas to protect the first surface. However, there has been little confirming evidence that conditions can be created to allow this propagation scheme. The highest pressure currently thought to be consistent with heavy ion beam propagation is

10^{-3} torr. This background pressure is not sufficient for first wall protection and is instead determined by the vapor pressure in sacrificial first surface reactor designs (see Section 3).

Light Ion Beams. Light ion beams (30 MeV Li and ∼1 MA per beam) cannot be transported in hard vacuum because the beam current exceeds the space charge limiting current and the radial space charge spreading current. A 1-10 torr gas background is the natural environment for light ion transport in reactor cavities to provide extremely good space charge neutralization. Ballistic transport in the presence of a gas is possible over distances dictated by the natural divergence of the beam, usually 1-2 meters. For longer standoff distances between the target and the diode or final focusing magnet, transport in the presence of a confining magnetic field is necessary. This magnetic field can be created by striking a pre-formed plasma channel discharge along the path from diode to target. A more speculative approach is to create an environment where space charge neutralization is very good but current neutralization is slightly incomplete. In this case the self-pinched ion beam is confined in its own magnetic field.

2.2.2. Target X Rays and Debris Ions

Following compression and ignition of a high gain ICF deuterium-tritium target, thermonuclear burn consumes 30-50% of the fuel in a time of picoseconds and a microexplosion results in the release of hundreds of megajoules (MJ) of energy in the form of neutrons, x rays and energetic ionic debris. Typically the 80% energy contribution of the neutrons from the D-T reaction is reduced to about 70% of the overall target yield due to scattering in the compressed fuel. The remaining 30% of the energy is divided between x rays and ionic debris. A generic target containing high-Z material has been used extensively for conceptual reactor studies and is shown in Figure 2 along with its x-ray spectrum (Böhne 1982). A low-Z target typical of direct drive ICF is shown in Figure 2 with its spectrum. The ion spectra for these targets are given in Table 1. These spectra are typically obtained from target design code calculations that follow the thermonuclear burn and target expansion

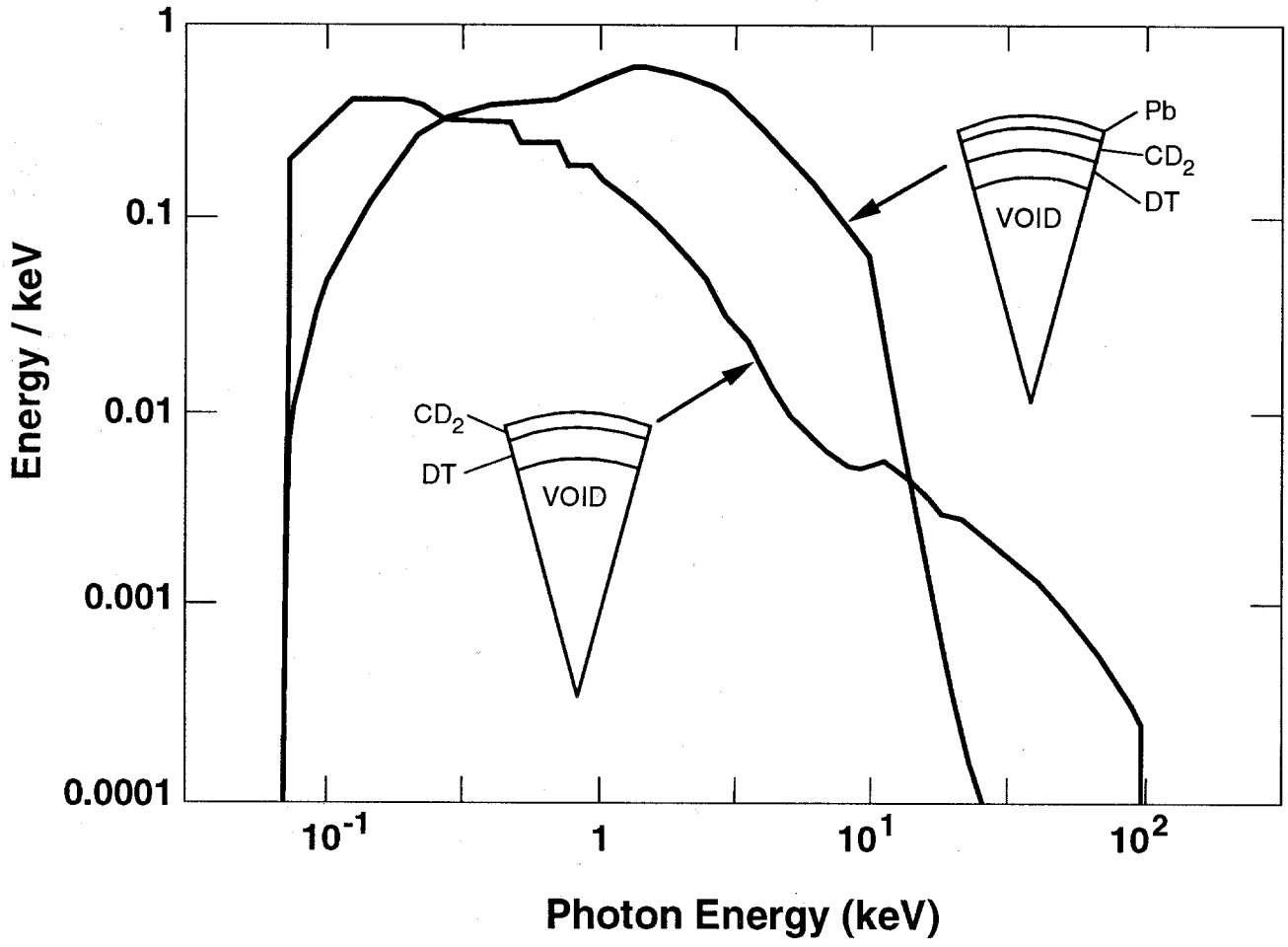

Figure 2. High gain, high-Z target and high gain, low-Z direct drive target and their time integrated x-ray emission spectra following thermonuclear burn.

Table 1. Target Debris Ion Spectra

	Direct Drive Target		High-Z Target	
	K.E./Ion (keV)	% of Ion Yield	K.E./Ion (keV)	% of Ion Yield
H	138	11.0		
D	94	7.2	1.93	0.24
T	140	10.5	2.89	0.36
He	188	5.3	3.8	0.30
C	1,650	66.0	11.1	18.79
Pb			198	80.30

(Moses 1977). The temporal profile of the x-ray emission from the high-Z target is shown in Figure 3 (Böhne 1982).

Target x rays are absorbed by the cavity gas largely through the photoelectric effect. This absorption depends strongly on the atomic number of the gas. Typical cross sections are shown in Figure 4 for helium, neon, and xenon. The x-ray fluence is great enough in relation to the number of gas atoms that the x rays can "bleach" the gas and remove all bound electrons before the target emission ceases (Moses 1985). This effect can make an otherwise opaque gas transparent to x rays emitted late in the burst. Failure to account for this results in inaccurate predictions of the x-ray flux incident on the first surface. Target x-ray emission and absorption in the surrounding gas occur over tens of nanoseconds. This is much shorter than either the ion expansion or the hydrodynamic response time.

Target ions slow down in the x ray preheated surrounding plasma by Coulomb interactions with bound and free electrons. This is a process complicated by ion stripping and electron reattachment. Ion ranges for mercury ions in neutral neon and xenon gases are shown in Figure 5.

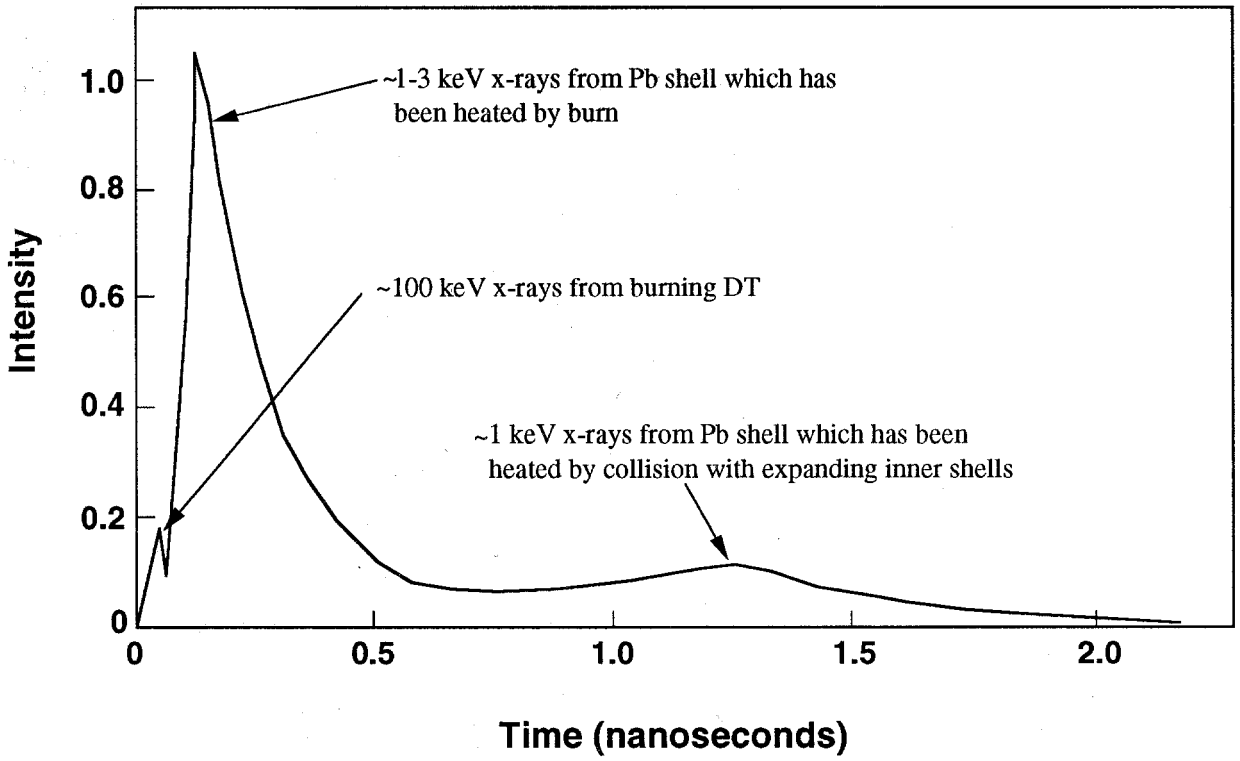

Figure 3. Temporal x-ray emission profile for high-Z target.

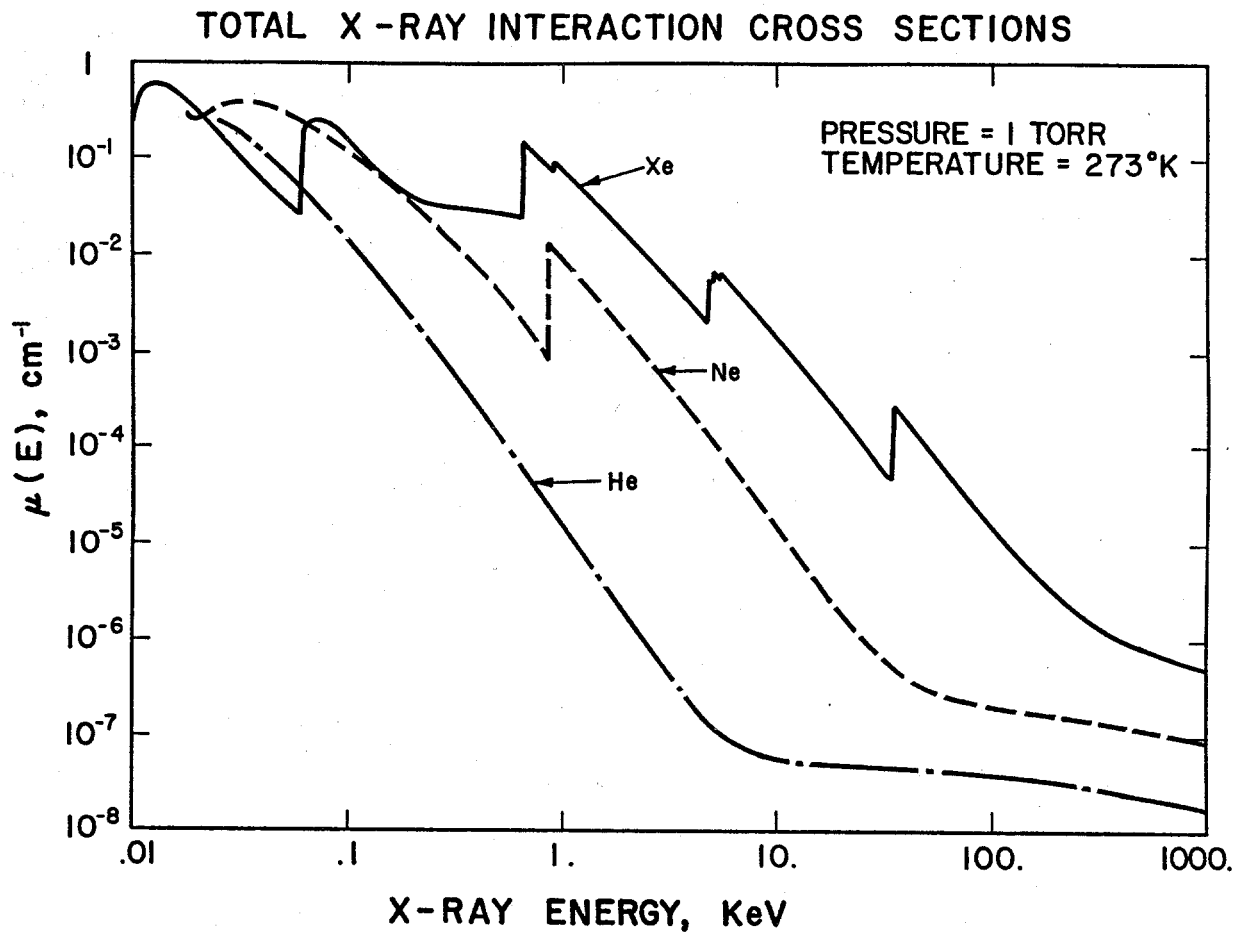

Figure 4. Photoelectric cross sections for helium, neon, and xenon.

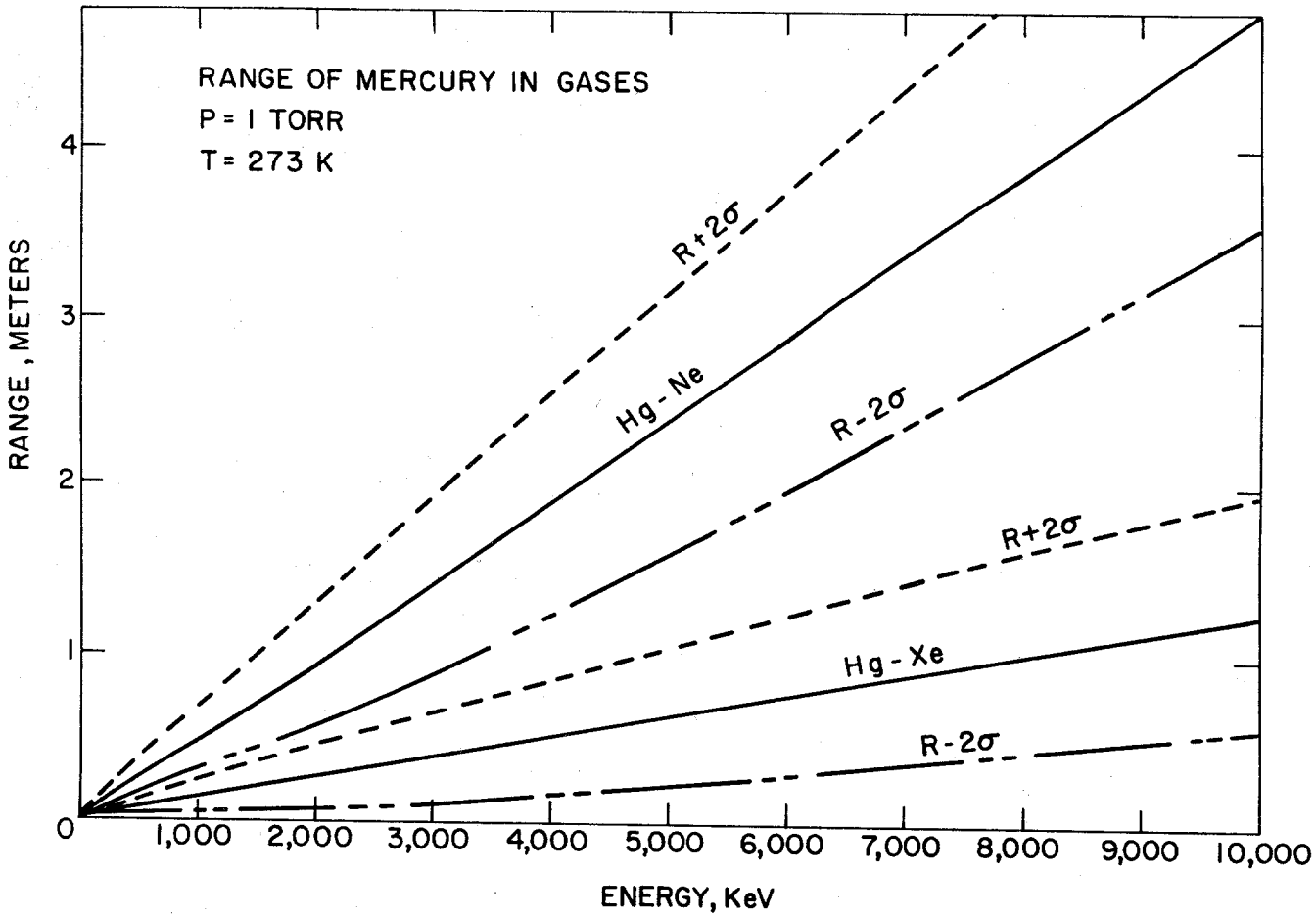

Figure 5. Range of mercury in neon and xenon gas, including the straggling effects.

2.2.3. Microfireball Dynamics

Absorption of the target x rays and ions transforms the cavity gas into a plasma microfireball, shown in Figure 6, with a temperature of 1-300 eV and density of about 10^{15} to 10^{17} cm^{-3} (Moses 1980; Bartel 1985; Bang 1991). This plasma is usually a noble element (He, Ne, Ar, or Xe) mixed with target ions. Under most of this temperature-density regime, Figure 6, this plasma is not in local thermodynamic equilibrium (LTE). For the LTE assumption to be valid the plasma density must be sufficiently high that all atomic processes–ionization, recombination, excitation, and de-excitation–are collisionally dominated (MacFarlane & Wang 1991). As seen in Figure 6, this assumption is rarely valid for ICF gas filled target chamber conditions. Emission to the first surface from the target chamber plasma is dominated by line radiation. The strength of this emission is difficult to determine because the plasma is optically thick to the lines but optically thin to continuum radiation. Because of this, the self-attenuation of the line radiation in their optically thick cores plays a critical role in both altering the atomic level populations and in significantly reducing the escaping radiation flux. Thus the local ionization and excitation population state densities are dependent upon the local radiation field (MacFarlane 1989). Figure 7 shows an example of a non-LTE spectrum emitted from an isothermal, 4 meter radius, spherical Ne cavity plasma (MacFarlane 1991).

If the cavity gas pressure is about 1 torr, then the energy deposition profile of target x rays and ions is gradual and the gas volume is more uniformly heated. If the gas pressure is tens of torr, then the ions are stopped in a small volume (10 cm radius) around the target. This hot, dense plasma expands outward via a supersonic radiation diffusion wave. As this wave slows it launches a shock wave that eventually reflects from the first surface (Zel'dovich & Raizer 1966).

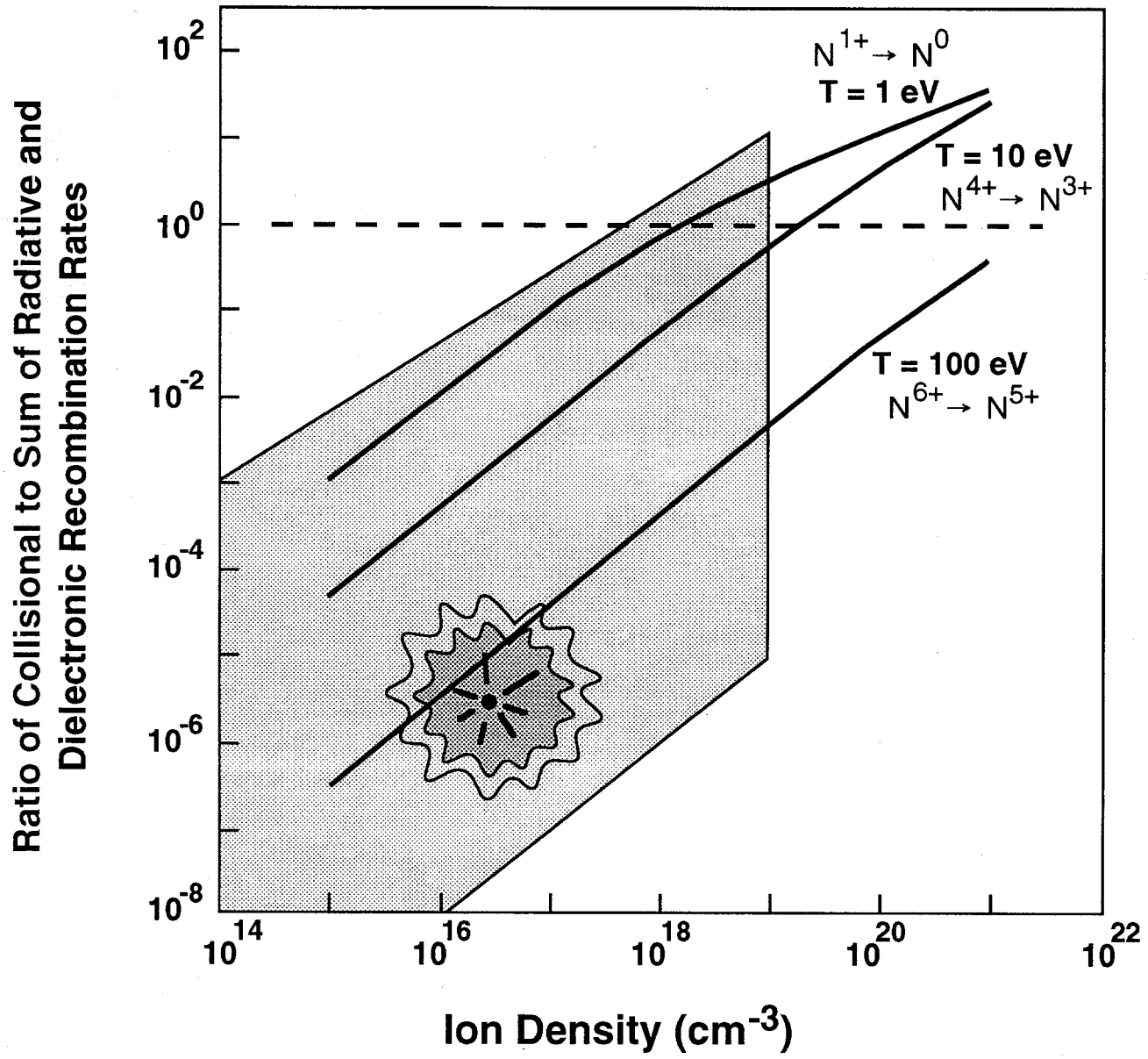

Figure 6. Reactor chamber plasmas are often not in radiative equilibrium. Ratio of collisional and two radiative recombination rates must be greater than one for equilibrium conditions. Target chamber conditions shown in shaded area. Dominant recombination rates plotted for three different temperatures for nitrogen.

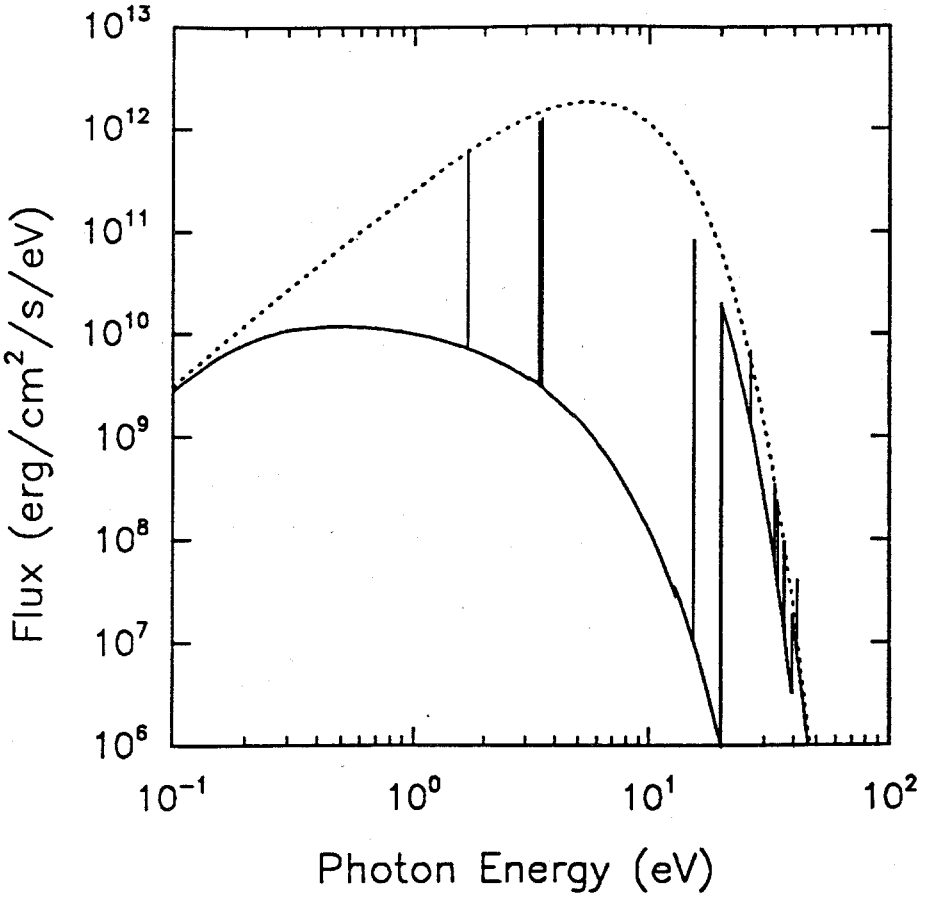

Figure 7. Radiation flux escaping a spherical neon plasma with T = 2 eV, n = 3×10^{16} cm^{-3}, and R = 4 meters. The dashed curve is the flux from a 2 eV blackbody.

2.2.4. First Surface Response

In the absence of a cavity gas, those surfaces in direct line-of-sight of the ICF target microexplosion experience an intense flux of x rays and expanding ionic debris. The x rays and ionic debris have ranges of one to tens of microns in solid matter. Energy deposited in this thin layer near the first surface facing the target can raise the temperature of the material in that layer by thousands of degrees. This results in ablation of the surface layer,

thermal fatigue and other deleterious effects that limit the lifetime of the structure (Peterson 1990).

The introduction of a gas in the target chamber protects the first surface from direct heating by the x rays and ionic debris from the ICF target microexplosion and reduces the temperature rise, as shown in Figure 8 (MacFarlane 1989; Peterson 1992). In the absence of a target chamber gas, the surface of the graphite in SIRIUS-T would reach the sublimation temperature of 4100 K and vaporize.

2.2.5. Cavity Clearing

After an ICF microexplosion and subsequent energy recovery, the reactor chamber conditions must be re-established in preparation for the next shot. After radiative transfer has removed 90% of the energy from the cavity gas, there still remains a hot gas exerting a high pressure on the reactor chamber. This high pressure can be used to advantage to self-pump the cavity while new cold gas is introduced to fully purge it. A timeline for a typical shot sequence is shown in Figure 9.

3. Sacrificial Plasma-facing Surfaces

3.1. Design Strategy

The idea of a sacrificial plasma-facing surface is to introduce a low melting point, low vapor pressure liquid metal (or molten salt) into the target chamber to absorb the short range x rays and ionic debris so they do not damage the first structural surface. The liquid also absorbs the neutrons and reduces the radiation damage to the vacuum vessel. The liquid metal or salt can be injected from the top of the reactor chamber as unconstrained jets that flow to a pool on the bottom (Monsler 1981). The jets disassemble into liquid drops and slugs due to isochoric heating by fusion neutrons on each shot (Blink 1985; Raffray 1986; Chen 1991; Chen 1991a). The liquid falls to the chamber pool under the influence of gravity. Another design approach is to constrain the liquid jets by porous

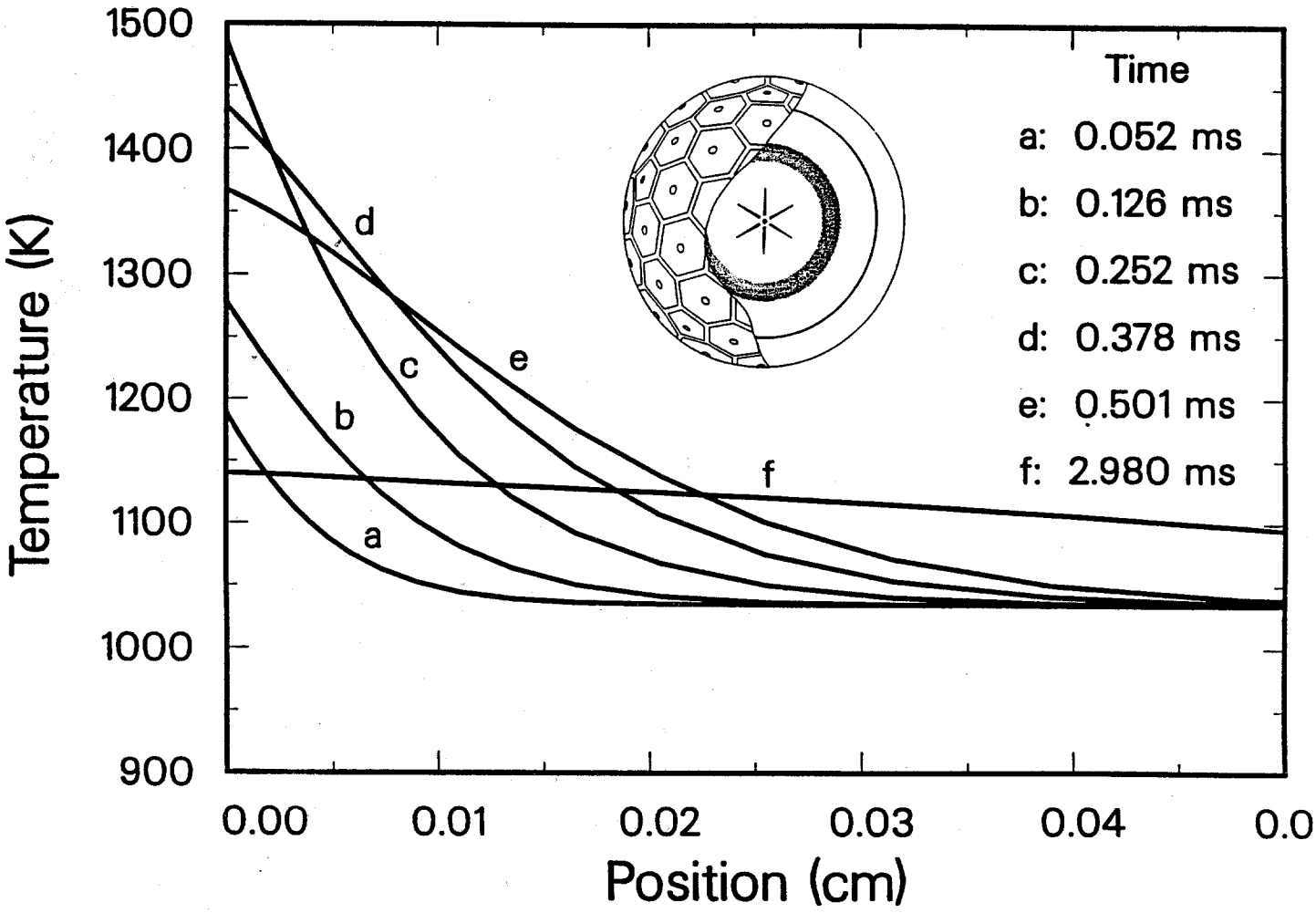

Figure 8. Temperature profiles in the carbon composite first wall of the SIRIUS-T reactor design following a 10 MJ target microexplosion. First surface was protected by 1 torr of xenon gas.

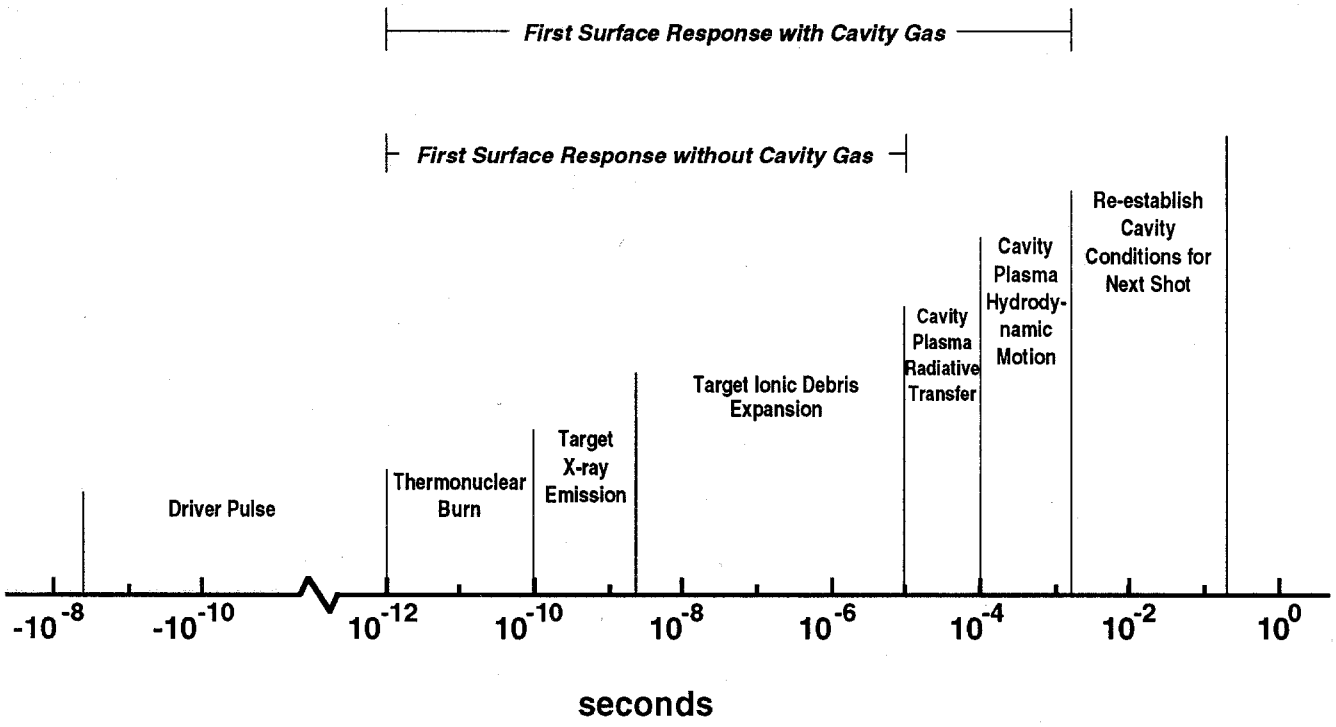

Figure 9. Timeline for a high gain microexplosion in a gas filled target chamber. Gas slows the first surface response by factor of 100, thus reducing thermal gradients.

tubes or sheets so that the bulk of the liquid does not disassemble by neutron heating (Bohne 1982; Sviatoslavsky 1991; Tillack 1991; Bourque 1992). The target microexplosion vaporizes and ionizes a thin film of the liquid on the surface of the porous material. This high-Z plasma expands and fills the reactor cavity and then reradiates its energy to the first surfaces, and recondenses onto the first surface over a much longer time scale than the original microexplosion, thus simultaneously reducing the instantaneous heat flux and returning the cavity to initial conditions (Orth 1986; Peterson 1986; Orth 1989). More recent approaches are to replace the liquid metal with liquid molten salt (Moir 1991; Moir 1992; Moir 1992a) or with ceramic sand-like particles that behave in bulk like a liquid (Pitts 1990; Pitts 1991; Tobin 1991).

The type of liquid metal or salt, the temperature at which it operates and the way that it is introduced into the target chamber are constrained by beam propagation, materials compatibility, tritium breeding capability, and recondensation requirements. A key issue of this reactor design concept is to re-establish the cavity conditions for the next shot. Large surface area structures and liquid sprays and droplets are utilized to enhance recondensation of the liquid (Bai 1991).

The OSIRIS heavy ion beam reactor design (Bourque 1992) (shown in Figure 10) used a tent-like woven SiC structure saturated with liquid molten salt, FLiBe, to protect the vacuum vessel from the expanding fireball and from neutron damage. The expanding blowoff plasma from this surface was directed downward by the geometry of the SiC surface. The vapor was then condensed on the liquid FLiBe pool and by sprays.

The LIBRA-LiTE light ion beam reactor design (Sviatoslavsky 1991) used a forest of woven SiC porous tubes (INPORTs) containing liquid lithium to protect the first structural surface from the blast of the microexplosion as shown in Figure 11. The lithium vapor ablated from the first rows of tubes fills the cavity and then flows through the array of tubes and is condensed on their large surface area as in a conventional heat exchanger.

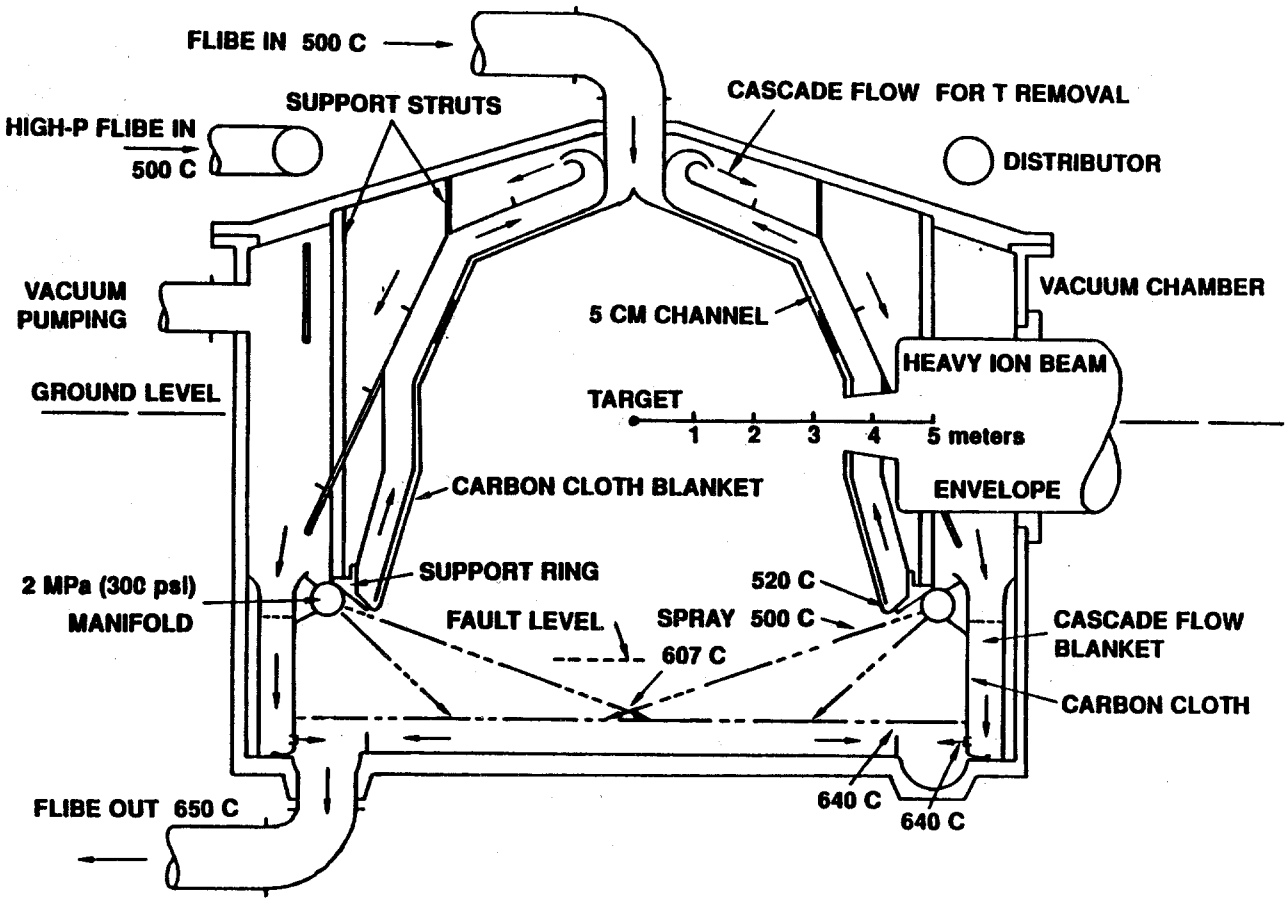

Figure 10. OSIRIS heavy ion beam reactor chamber.

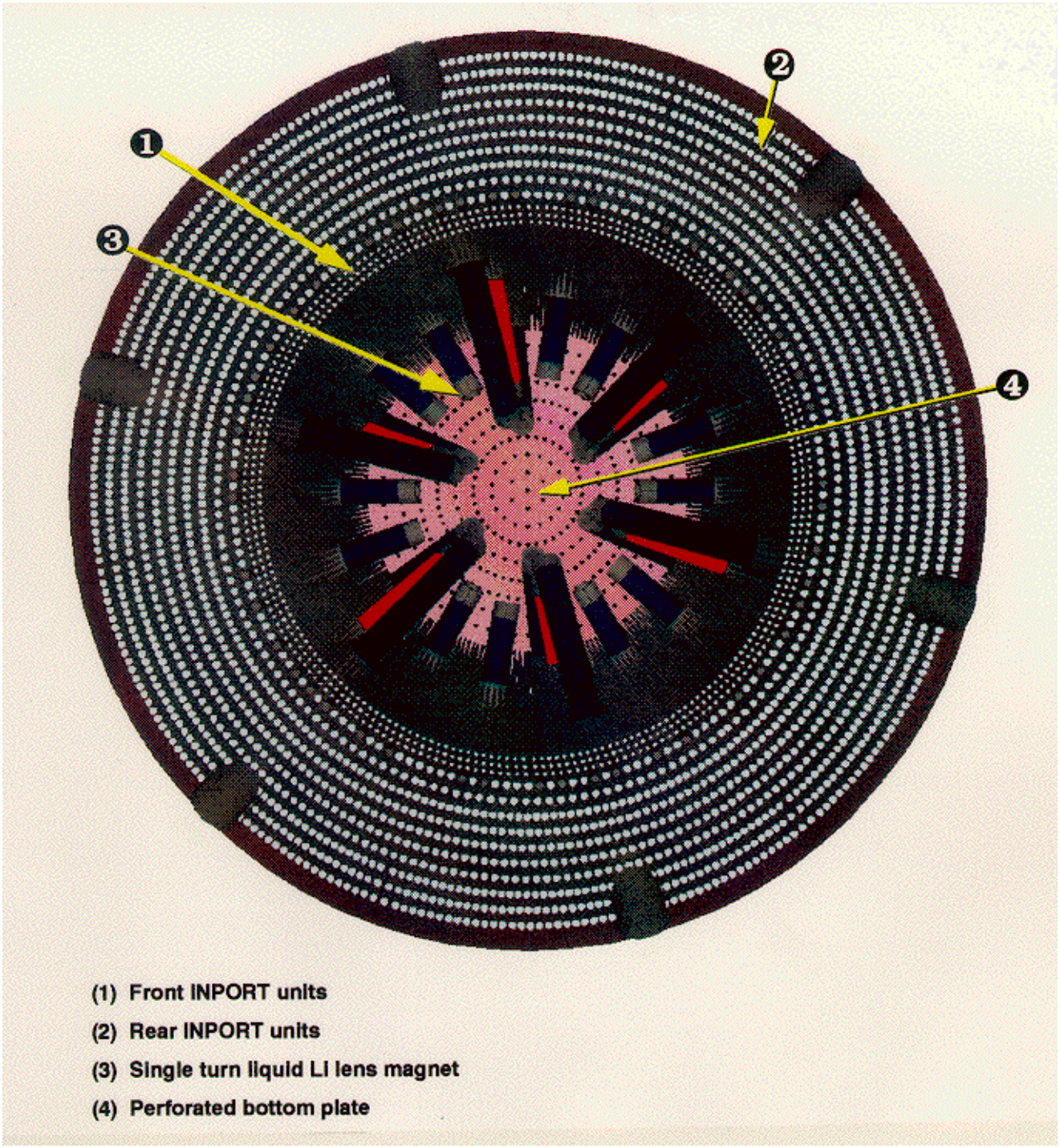

Figure 11. LIRBA-LiTE light ion beam reactor chamber viewed from the top. Rows of porous SiC tubes contain liquid lithium and are wetted on the outside to protect them from the target x rays and ionic debris.

3.2. Phenomenology

Again, design points are chosen to satisfy offsetting physical constraints. The physical phenomenology of beam propagation in a vapor, ablation of liquid and recondensation time of vapor, thermo-mechanical response of porous tube and sheet-like structures in the reactor cavity, and liquid flow in bulk and thin films must be understood to model these reactor schemes. An important governing relation is the vapor pressure of the liquid as a function of temperature. This is shown in Figure 12.

3.2.1. Beam Propagation

Laser Beams. Lasers require pressures below about 10^{-3} torr to avoid any breakdown phenomena. Figure 12 shows that this pressure is easily achievable for all temperatures that are consistent with materials compatibility.

Heavy Ion Beams. Vapor pressures below 10^{-3} torr are thought to be acceptable for heavy ion beam propagation. Operating temperatures below 900 K for lithium-lead are required as shown on Figure 12.

Light Ion Beams. Light ion beams require pressures of about 1 torr or greater for space charge and current neutralization. This pressure is much too high to achieve from metal vapor alone. For light ion beams, a noncondensable gas must be introduced into the cavity to provide the background medium for beam propagation. This gas can be helium if desired, because the liquid metal will serve as protection from x rays and ionic debris.

An issue for all beam propagation schemes is droplets in the beam path. The spatial relation between droplet sources and the beam paths and gravitational acceleration determines the importance of this problem. Another issue for all propagation schemes is threading the beams through the forest of liquid jets or tubes in the reactor cavity.

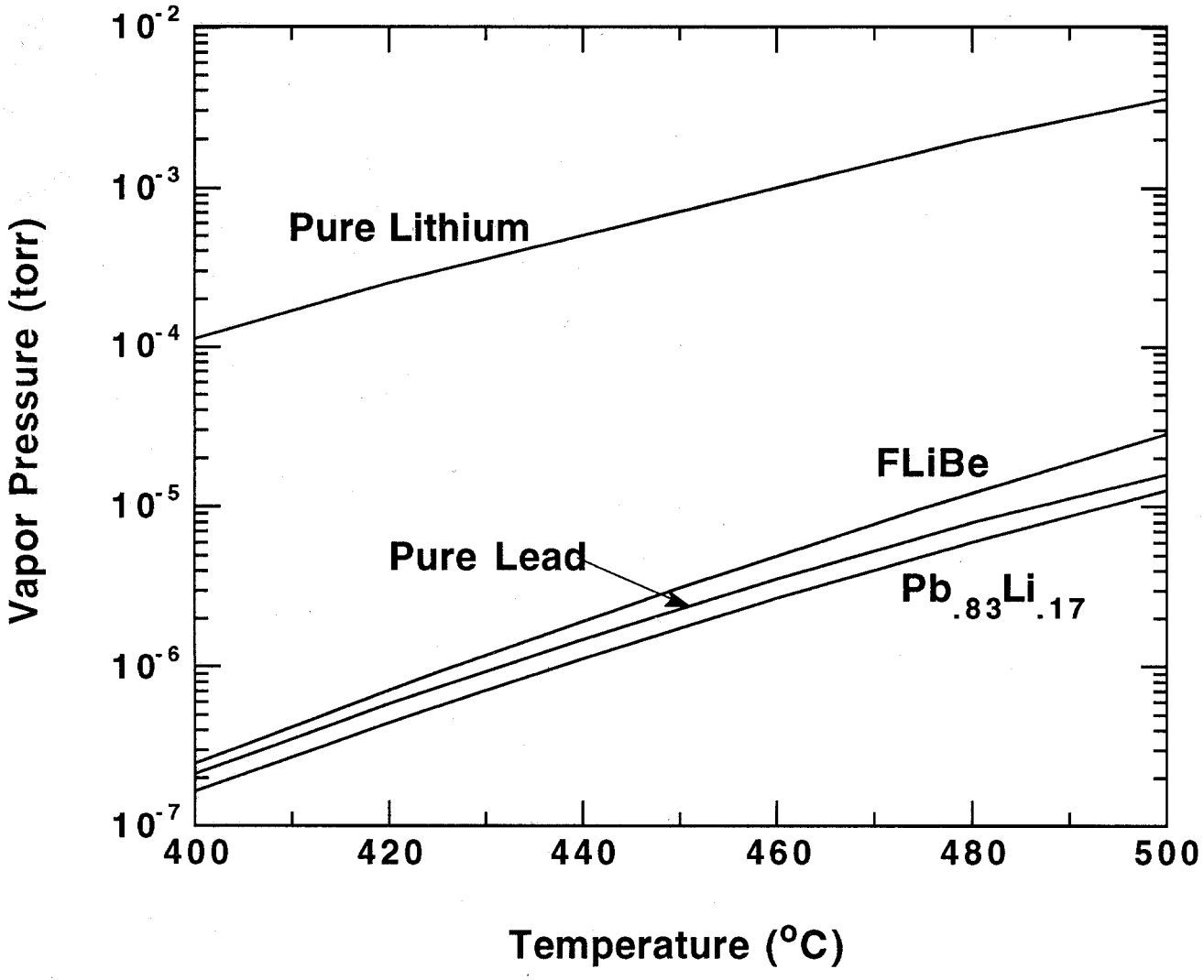

Figure 12. Vapor pressure versus temperature for common liquids used for plasma-facing surface protection.

3.2.2. Unconstrained Liquid Response to Microexplosion

Following ignition and thermonuclear burn the target x rays vaporize and ionize the surface of the liquid jets facing the target. This material expands inward toward the target position. The expanding ionic target debris intercepts the blowoff from the face of the jets and heats this expanding plasma even more. The neutrons volumetrically deposit energy in the jets. (The 14 MeV neutron mean free path in solid matter is about 10 cm.) This rapid energy density change causes the jets to disassemble into droplets and slugs of liquid. The target chamber is filled with a three phase combination of plasma, vapor and liquid droplets and slugs shown in Figure 13. The mass, momentum, and energy exchange between these three components and the acceleration of gravity pulling the liquid to the chamber floor determine the clearing time of the cavity for the next shot. This is a very complex, three dimensional, multiphase phenomenon.

3.2.3. Constrained Liquid Response to Microexplosion

The phenomena is simplified when the liquid is constrained by a porous material. The liquid film on the plasma-facing surface is vaporized and ionized and expands inward and is intercepted by the ionic debris in the same way as in the unconstrained case. But the bulk liquid does not disassemble as a result of neutron heating because it does not have a free surface. The cavity clearing time is determined by the recondensation of the vapor and plasma on fixed surfaces within the cavity and the acceleration of gravity is not an issue. The condensation time is dictated by the heat transfer at the condensation surfaces and by mass transfer of the plasma from the cavity to these surfaces (Pong 1985). The response of the constraining material to the plasma blow-off from target x-ray deposition (Engelstad 1985) and the radiation damage of the constraining material are new considerations in this concept. These components are estimated to have a one year lifetime before replacement is required. Reactor chambers are designed to allow easy replacement.

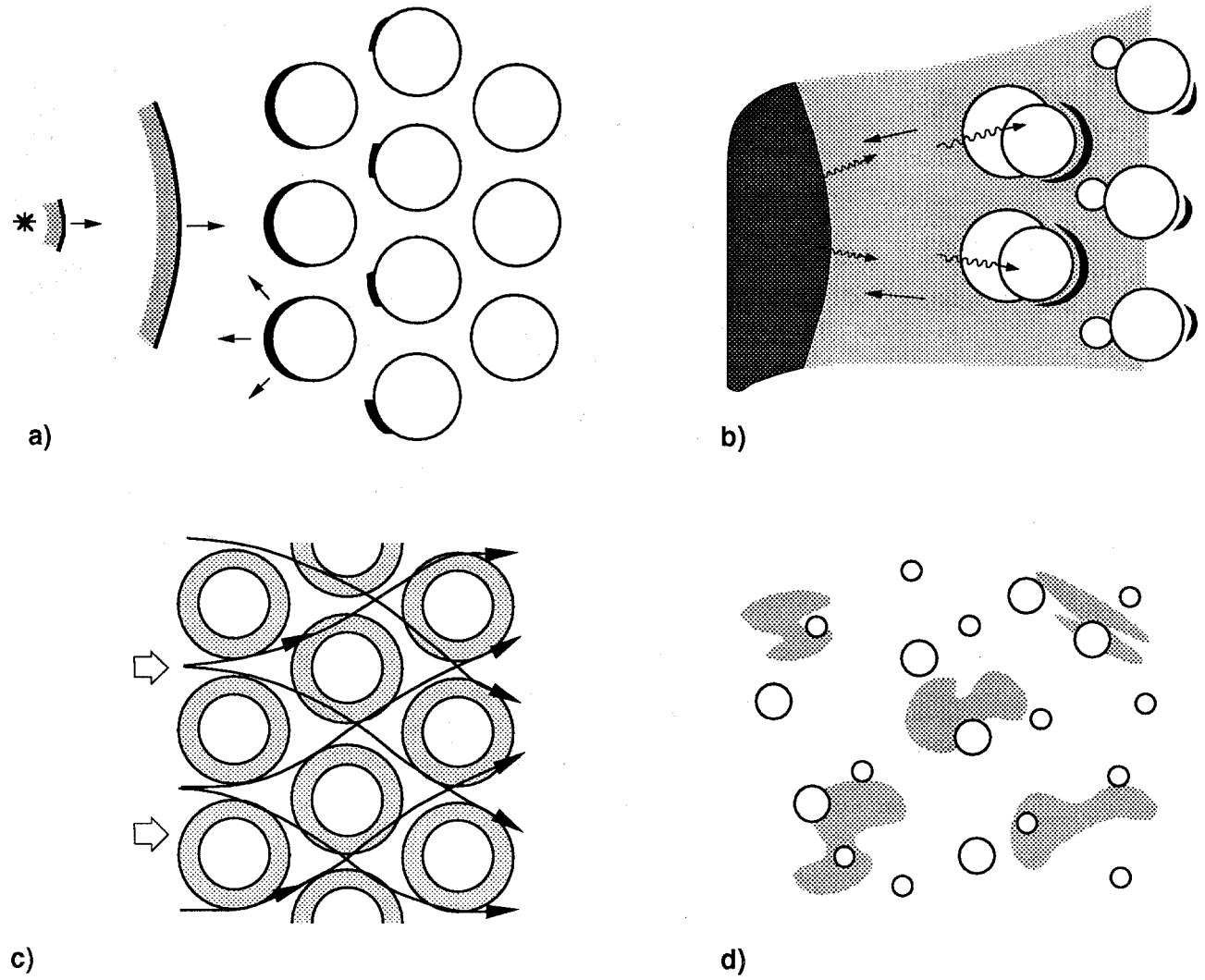

Figure 13. Schematic diagram of target chamber phenomena in liquid jet protected first surface design.

3.2.4. Solid Granule First Surface Response to Microexplosion

Sand-like solid granules can be held against the structural wall using angular acceleration by rotating the whole structure (Pitts 1990; Pitts 1991). These particles enter the chamber at the ends and flow toward the equator, where they are ejected into a heat recovery system. The surface of the granules facing the exploding target is ablated, just as in the liquid metal case. This plasma material expands and fills the target chamber and must recondense before the next shot. The individual granules that experience this blowoff are stressed by an equal and opposite shock wave. This can fracture the granules into fines that must be recovered and separated from the bulk of the material.

4. Physical and Numerical Models

4.1. Target – Cavity Coupling

4.1.1. Ion Deposition

Calculation of target debris ion stopping by the target chamber fill gas must consider the increase in temperature of the gas due to the energy deposition. Even in cold material, the stopping of ions must be calculated with models that are valid for the target debris ion energy. At finite gas temperatures, the ion stopping is affected by modifications to the bound electrons and by the addition of free electrons. The stopping power of heated material has been found to be significantly higher than in cold material (Mehlhorn 1981; Mehlhorn 1983).

Contributions to ion stopping can be divided between bound electron and free electron effects. The bound electron contribution consists of electron and nuclear parts. The nuclear ion stopping power can be expressed for both cold and finite temperature conditions as:

$$\left(\frac{dE}{dx}\right)_{nuc} = \rho C_n \epsilon^{1/2} \exp(-45.2(C_n'\epsilon)^{0.277}) \text{ [MeV/cm]} \quad (1)$$

where,

$$C_n = 4.14 \times 10^6 \left(\frac{A_1}{A_1 + A_2}\right)^{3/2} \left(\frac{Z_1 Z_2}{A_2}\right)^{1/2} (Z_1^{2/3} + Z_2^{2/3})^{-3/4} \tag{2}$$

$$C_n' = \frac{A_1 A_2}{A_1 + A_2} \frac{1}{Z_1 Z_2} (Z_1^{2/3} + Z_2^{2/3})^{-1/2} \tag{3}$$

$$\epsilon = E/A_1 \text{ [Mev/amu]} \tag{4}$$

and Z_1 is the atomic number of the projectile ion, Z_2 is the atomic number of the stopping medium, A_1 is the atomic weight of the projectile ion A_2 is the atomic weight of the stopping medium.

The electron part of the bound electron contribution must be calculated within a model that is chosen on the basis of ion energy. At high ion energy, the Bethe model accounts for both ionization and atomic excitations:

$$\left(\frac{dE}{dx}\right)_{Bethe} = \frac{4\pi N_0 Z_{eff}^2 \rho e^4 Z_2}{m_e c^2 \beta^2 A_2} \left(\ln \frac{2 m_e c^2 \beta^2 \gamma^2}{\bar{I}} - \beta^2 - \frac{\sum_i C_i}{Z_2} - \frac{\delta}{2}\right) \tag{5}$$

where, Z_{eff} is the effective charge of the projectile ion, N_o is Avogadro's number, ρ is the mass density of the stopping medium, and β is the projectile ion speed divided by the speed of light in vacuum, c. δ is a polarization correction term, m_e is the electron rest mass, $\bar{I}$ is the average ionization potential, $\sum C_i/Z_2$ is the sum of the effects of shell corrections on the stopping power, and e is the electronic charge. The polarization term is important at ultra-relativistic projectile energies and not important at ICF target chamber conditions (Jackson 1962). Shell corrections are important at low projectile energies. Anderson and Ziegler (Andersen & Zielger 1977) have tabulated shell correction coefficients for proton stopping, which can be applied to higher mass projectiles with the same energy per unit mass. The effective charge state of the projectile ion can be estimated to be (Brown & Moak 1972;

Miller 1982)

$$Z_{eff} \approx Z_1 \left(1 - 1.034 \exp -\frac{137.04\beta_i}{Z_1^{0.69}}\right). \tag{6}$$

The Bethe formula, even with the inclusion of shell corrections, is not appropriate at low ion energies. The LSS model includes the effects of elastic Coulomb collisions and is based on a Thomas-Fermi model, which makes it more valid at low ion energy. The LSS stopping power due to atomic electrons can be expressed as:

$$\left(\frac{dE}{dx}\right)_{LSS} = C_{LSS}\sqrt{E} \tag{7}$$

where,

$$C_{LSS} = 2.498K\frac{E_L^{1/2}}{R_L}\ [\mathrm{keV}^{1/2}/\mu\mathrm{m}] \tag{8}$$

$$E_L = \frac{(1+A)Z_1Z_2e^2}{Aa}\ [\mathrm{keV}] \tag{9}$$

$$a = 0.4683 \times 10^{-8}(Z_1^{2/3} + Z_2^{2/3})^{-1/2}\ [\mathrm{cm}] \tag{10}$$

$$R_L = \frac{(1+A)^2}{\pi ANa^2}\ [\mathrm{cm}] \tag{11}$$

$$A = A_2/A_1 \tag{12}$$

$$K = \frac{0.0792Z_1^{2/3}Z_2^{1/2}(1+A)^{3/2}}{(Z_1^{2/3} + Z_2^{2/3})^{3/4}A_2^{1/2}} \tag{13}$$

and N is the target atom number density in cm^{-3} and A_1 is the atomic weight of the projectile ion. The cold stopping power is calculated as

$$\left(\frac{dE}{dx}\right)_{bound} = min\left[\left(\frac{dE}{dx}\right)_{Bethe}, \left(\frac{dE}{dx}\right)_{LSS}\right] + \left(\frac{dE}{dx}\right)_{nuc} . \tag{14}$$

As a material heats, the contribution of free electrons to the stopping power becomes important. Free electrons are released through ionization of the atoms of the stopping medium. The calculation of ionization of the stopping medium can be performed within an equilibrium approximation, for example using the Saha method discussed in the section on equations of state. If the ion power density is high, the atoms in the stopping medium will not be in equilibrium as the projectile ions depopulate particular shells of the stopping atoms. In this case, a detailed calculation of the stopping power from each atomic shell may be called for. The degree of ionization will affect $\bar{I}$ in the Bethe formulation. The average ionization potential is a function of the atomic structure of the stopping medium and is defined by the relation

$$\ln \bar{I} = \frac{\sum_n f_n \ln E_n}{Z} , \tag{15}$$

where E_n is the energy difference and f_n is the oscillator strength of transition n. The allowed transitions change as the atoms are ionized, and as the projectile ion energy changes. This implies that $\bar{I}$ is a function of the temperature of the stopping medium and the ion energy. In fact, a direct calculation based on this definition is not practical because the oscillator strengths are often not known. $\bar{I}$ has been measured in some situations and it can be scaled from these results for low Z. For high Z, more detailed atomic models are required.

The contribution of free electrons to the stopping power is important and can be written in a form that includes the contributions from binary collisions and collective plasma excitation:

$$\left(\frac{dE}{dx}\right)_{free} = \frac{\omega_p^2 Z_{eff}^2 e^2}{c^2 \beta^2} G(y_e) \ln \Lambda_{free} \tag{16}$$

where,

$$G(\zeta) = erf(\zeta^{1/2}) - 2\sqrt{\frac{\zeta}{\pi}}\, e^{-\zeta} \tag{17}$$

$$y_e = \left(\frac{m_e c^2 \beta^2}{2T_e} \right)^{1/2} , \tag{18}$$

ω_p is the electron plasma frequency, and $\ln \Lambda_{free}$ is the free electron Coulomb logarithm. The Coulomb logarithm should be calculated with some care because the stopping medium may be a weakly ionized plasma (Mohanti 1990). A similar formalism exists for the stopping due to binary Coulomb collisions with plasma ions, but this is only important when the stopping ion thermal velocity is comparable to the projectile ion velocity, a condition that does not usually occur in ICF target chambers.

The effect of the temperature of the stopping medium on the stopping range is shown in Figure 14. One can see that at low temperatures, the range shortens with increasing temperature. This is due to the increased stopping by free electrons. As the temperature increases, more free electrons are created by increased ionization. The function G(y) in the free electron stopping power formula is proportional to the Coulomb stopping power and reaches a maximum when the electron thermal velocity in the stopping medium is equal to the projectile velocity. At low temperatures, when the electron thermal velocities are less than the projectile ion velocity, G(y) is increasing with temperature, which contributes to increased stopping powers. At high temperature the range increases with temperature. When the electron thermal velocity in the stopping medium is greater than the velocity of the projectile ion, G(y) decreases with temperature.

4.1.2. Electron Deposition

Generally, electrons emanating from the target microexplosion are supposed to move along with the the target debris ions, as charge neutrality would require. If this is the case the total energy in electrons, E_e can be related to the energy in ions, E_i, by the expression

$$E_e \approx \frac{m_e Z}{m_i} E_i. \tag{19}$$

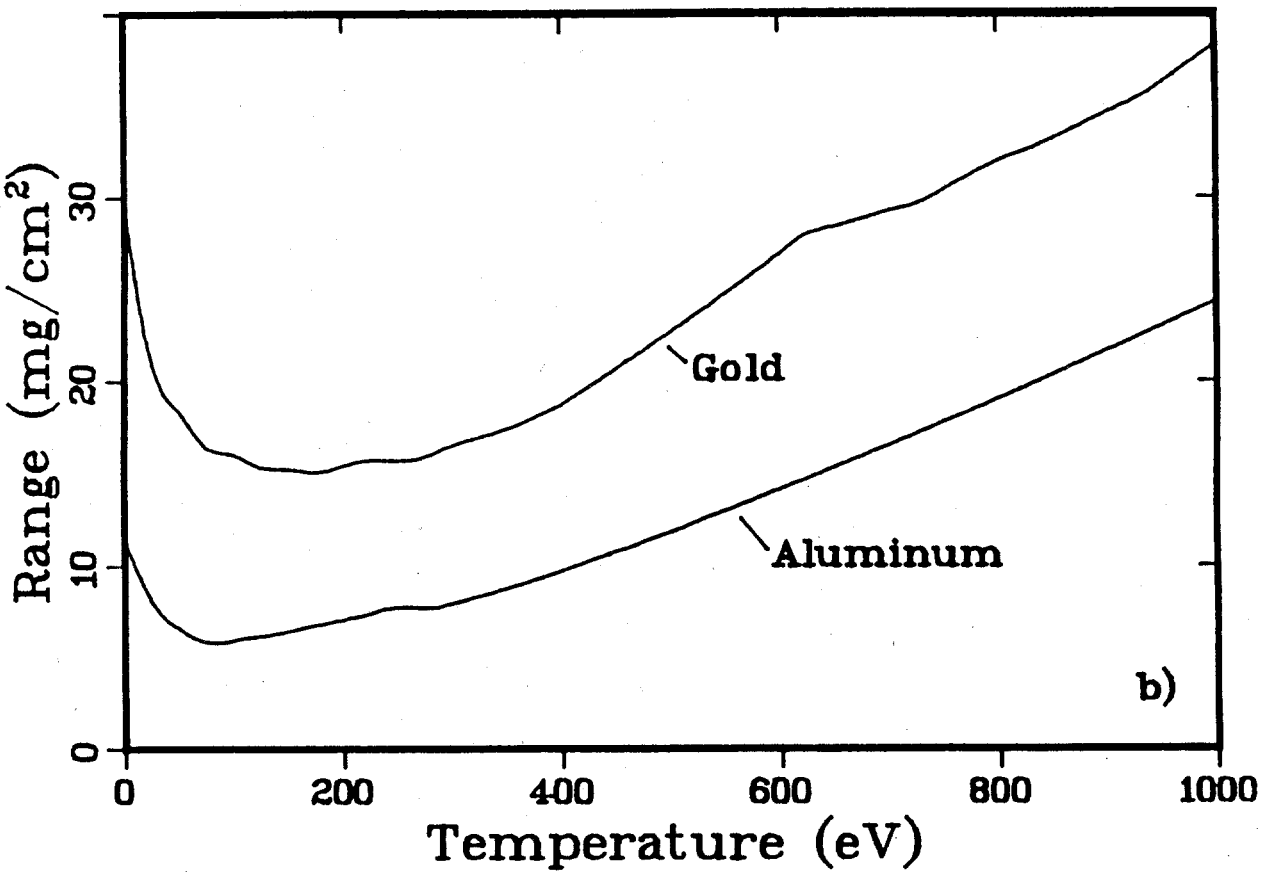

Figure 14. Range of a 2 MeV proton versus material temperature in aluminum and gold (Mehlhorn 1981).

In this expression Z is the average charge state of the debris plasma. From this, E_e is more than three orders of magnitude less than E_i and is probably not important to the target chamber response. If electrons are emitted by the target at similar energies to the ions and a charge separation is permitted to grow, then one must calculate the deposition of these electrons into the target chamber fill gases and structures.

The stopping of electrons in matter differs from the stopping of ions in the importance of radiative processes (Bremsstrahlung and pair production). The excitation and ionization contributions to the stopping power can be calculated using similar formalism to that for ions. As the energy of the electrons increases, radiative processes become relatively more important. The relativistic expression for the stopping power due to radiation for electrons with energy $\gamma m_e c^2$ in material with atomic number, Z, is

$$\left(\frac{dE}{dx}\right)_{rad} \simeq \left[\frac{16}{3} N \frac{Z^2 e^2}{\hbar c}\left(\frac{e^2}{m_e c^2}\right)^2 \ln\left(\frac{\lambda 192}{Z^{1/3}}\right)\right] \gamma m_e c^2 \,. \tag{20}$$

For the very low energy electrons that local charge neutrality in the debris plasma would require, the stopping power depends on very complicated interactions with the bound electrons in the stopping medium. Detailed quantum mechanical calculations are required to perform this calculation. Luckily, it is probably not important for the reasons stated.

4.1.3. X-Ray Deposition

The transport and deposition of target x rays can be treated in the same way as for any photons. However, the target x rays exhibit and generate phenomena that can often be neglected for photons in target chambers. The target x rays are very intense near the target because the pulse width is very short. This leads to a modification of the medium. Atomic levels in the medium can be severely altered by x-ray absorption. The levels normally responsible for absorption can become depleted, leading to a significantly reduced absorption

cross section. Therefore, to accurately calculate the x-ray deposition, the changes in the populations of atomic levels must be considered.

4.2. Material Response

4.2.1. Phase Transitions

Target x rays and debris ions can heat liquid or solid plasma-facing surface material to the point that phase transitions occur. X rays and ions can heat the material in depth. This situation can be modeled in alternative ways. A kinetic model can be used to calculate the rate at which atoms, molecules, or clusters are evaporated from the solid or liquid surface. A volumetric model can be used to predict how much material is converted from one phase to another. Both models require calculation of energy deposition and heat conduction in the material, since the power balance between sources and losses is critical to the amount of material that experiences phase transitions. Also, the latent heat of phase transition must be carefully removed from material undergoing a transition.

Kinetic theory, based on standard statistical mechanics, can calculate the rate that atoms leave a surface as another phase. Versions of kinetic theory can calculate evaporation, sublimation, and melting. For evaporation or sublimation, the mass ablation rate can be written as

$$\dot{m} = \left(\frac{m_a}{2\pi T_s}\right)^{1/2} \left(P_{sat}(T_s) - P_g\right) , \tag{21}$$

where T_s is the surface temperature of the evaporating material, m_a is the atomic mass, P_{sat} is the saturation vapor pressure at T_s, and P_g is the pressure of vapor in contact with the surface. P_{sat} is a function of the energy required to separate an individual atom, molecule, or cluster of atoms from the surface. The separation energy per unit mass will be much lower for molecules and clusters, leading to a higher P_{sat} and a greater mass ablation rate. P_{sat} has been determined for many materials, usually in equilibrium. These can be used when they are relevant, though they are often not relevant for ICF target chamber conditions. P_{sat} can

be calculated as:

$$P_{sat} = P_o \exp\left(\frac{-\Delta H_v}{kT_{vap,o}}\left[1 - \frac{T_{vap,o}}{T_s}\right]\right) , \tag{22}$$

where ΔH_v is the latent heat of vaporization and $T_{vap,o}$ is the vaporization temperature of P_o.

Volumetric models can be useful in cases where the volumetric energy deposition is rapid enough that the resulting hydrodynamic motion is insignificant during the deposition pulse. This is often the case in ICF target chambers. A sample deposition pulse is shown in Figure 15. The energy density required for phase transition, ε_t, and the sensible heat required for the material to be at the phase transition temperature, ε_{sens}, are both marked in the figure. In a volumetric phase transition model, material with energy density greater than ε_t undergoes a phase transition, material with energy density less than ε_{sens} does not. There is material with energy density between ε_{sens} and ε_t, whose condition is unclear. One approach is to treat that material by re-distributing the energy so that all material that was in this condition is either at ε_t or ε_{sens}. Material which is now at ε_t would then make the phase transition. This approach calls for arbitrary heat transfer and is, therefore, unsatisfying, so other treatments could be explored. Comparing calculations with experiment would determine the correct treatment.

4.2.2. Fragmentation of Liquids and Solids

Target emanations can rapidly heat target chamber structures, causing them to rapidly expand and fragment. The size of resulting fragments is determined by the kinetic energy gained by the material during rapid expansion and the energy per unit surface area that the fragments must have (Grady 1982). For a liquid this energy per unit area is the surface tension; for a solid it is the fracture toughness. The fragmentation of both liquids and solids can occur in ICF target chambers. In the HYLIFE reactor design, liquid metal jets are used to protect the target chamber wall from target x rays, ions and neutrons. The

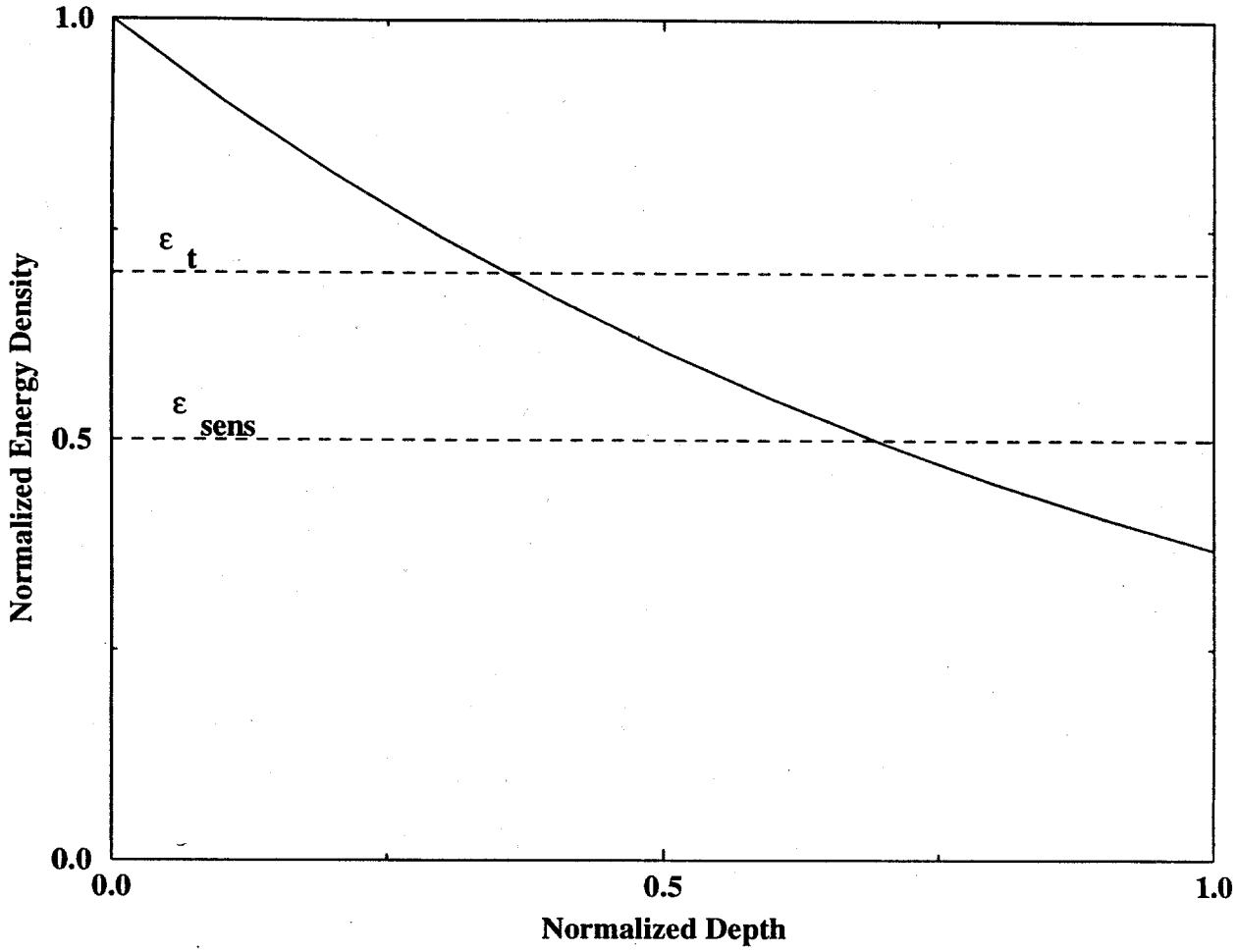

Figure 15. Schematic energy density profile in target chamber material. ε_t is the energy density required for phase transition. ε_{sens} is the energy density required for the material to be at the transition temperature.

energy deposition can lead to fragmentation of the jets by rapid expansion overcoming the surface tension of the jets (Blink 1985). In the HIBALL reactor, a liquid metal film coats the surface of tubes, protecting them from the x rays and ions. The film rapidly expands and could overcome the energy of cohesion between the tubes and the film, causing the film to splash off. As a final example, in any one of a variety of Laboratory Microfusion Facility designs various solid structures may be inserted into the target chamber. These will be rapidly heated and expanded, creating enough kinetic energy to overcome the fracture toughness of the solid (Peterson 1991).

In all cases, the rate of expansion is critical to the fragmentation process. Also, the deposition time is short compared to the hydrodynamic expansion time, so one cannot assume that the material completes its full expansion by the end of the deposition pulse. One may calculate the pressure generated in the material by the deposition and the expansion velocity from that. The most reasonable equation of state to calculate the pressure in all of these cases is the Grüneisen formula:

$$P = \Gamma \frac{E}{V} \, . \tag{23}$$

Here, Γ is the Grüneisen coefficient, and E/V is the energy per unit volume. Once one knows the pressure the ultimate velocity and kinetic energy of the material can be estimated. The size of the resulting fragments will depend on this, on the fracture toughness or surface tension of the material, and the geometry of the structure.

4.2.3. Condensation

The condensation of material that has been vaporized from target chamber structures and from the target itself, plays an important role in the design and operation of an ICF target chamber. In a power reactor target chamber design, the rate that vaporized material recondenses determines the repetition rate.

The condensation is affected by the rate at which atoms or molecules can reach the first wall and by the ability of atoms or molecules reaching the wall to be adsorbed. The presence of noncondensable species must be considered, as they can slow the diffusion of the condensing material. A layer of noncondensable gas builds up between the condensing surface and the vapor, which slows the movement of the vapor. There have been kinetic models developed (Koffman 1983; Soga 1982; Pong 1985; Labuntsov 1979) that take into account the very important non-Maxwellian distribution function that the vapor atoms and molecules have in the region near the condensing surface. The effect of the noncondensable gas on condensation rate is demonstrated in Figure 16 (Pong 1985) for lead vapor and several species of gas. It is currently impractical to include these kinetic models in the radiation-hydrodynamics codes, but a noncondensable scale factor, β, on the condensation rate can be useful. The condensing surface may not be flat and may therefore have a larger effective area for condensation. Therefore, the condensation rate should be scaled by an area factor, A_c. Only a fraction (the sticking fraction, α) of the vapor atoms or molecules that reach the condensing surface actually are adsorbed. The mass condensation rate can be calculated with a version of equation 21 that has been suitably modified to include these effects:

$$\dot{m} = \left(\frac{m_a}{2\pi T_s}\right)^{1/2} \left(P_{sat}(T_s) - \alpha\beta A_c P_g\right). \tag{24}$$

This is the net condensation or evaporation rate and T_s is the temperature on the surface of the condensed material, which is assumed to be equal to the temperature of the vapor in contact with the surface. When P_{sat} is less than $\alpha\beta A_c P_g$, equation 24 calculates the mass condensation rate.

Nucleate condensation occurs when the vapor temperature falls below the local vaporization temperature. This can occur in a target chamber plasma when material vaporized from a surface cools due to expansion. In such a situation, the condensation takes place in the vapor volume by initiating droplet formation on nucleation sights. The

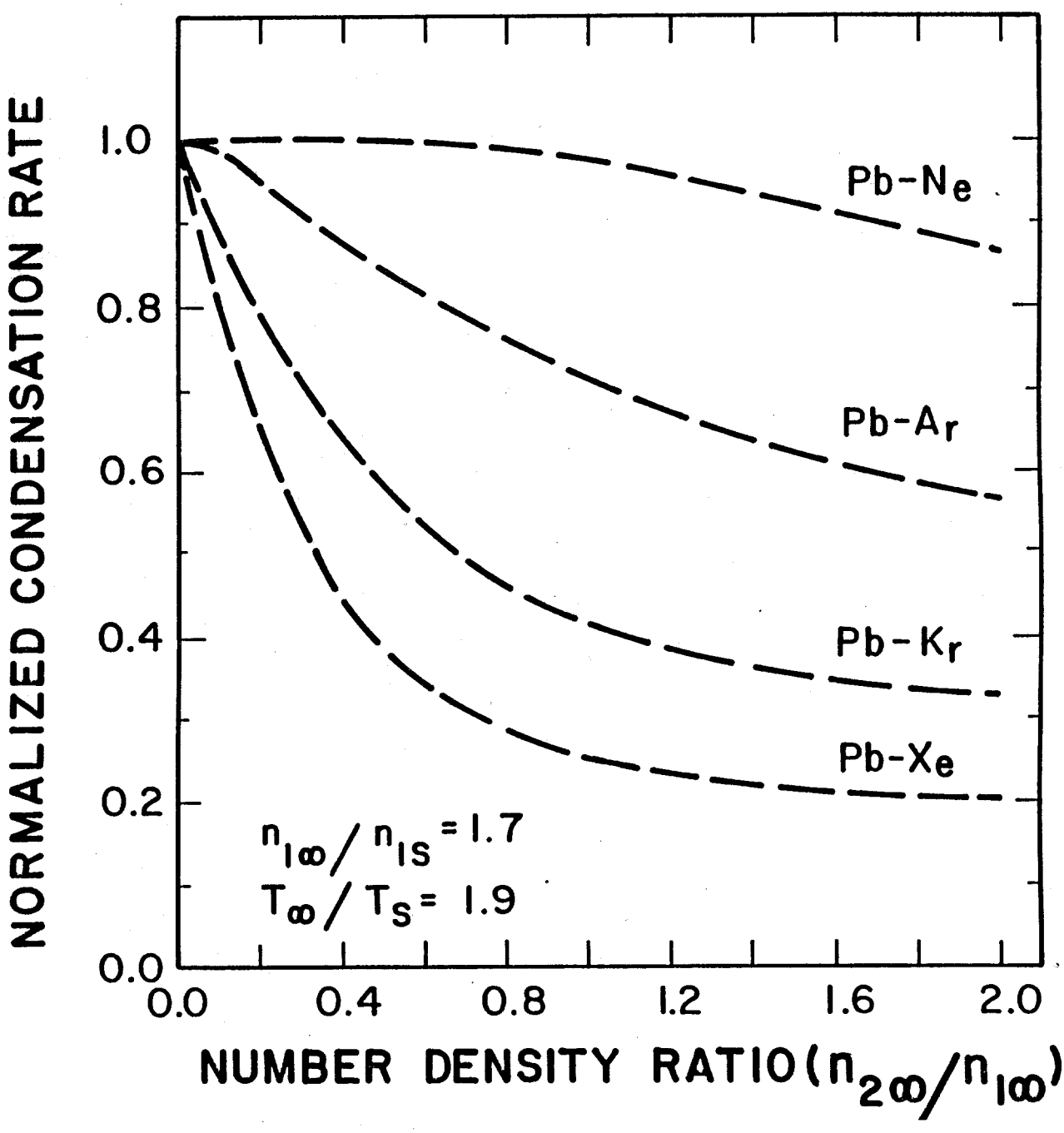

Figure 16. Influence of noncondensable gas concentration on the condensation rate of lead vapor for several species of noncondensable gas.

rate of condensation will depend on the nucleation sight density and the droplet growth rate (Bang 1991).

4.3. Hydrodynamics

The motion of the target chamber fill gases and plasmas and the vapors created by target emanations is critical to understanding target chamber phenomena. Plasma and vapor motion is essential to pressure loading and to condensation of vaporized material. Usually, one can assume the motion to be governed by the equations of hydrodynamics, that is, the mean free path for collisions between plasma atoms or molecules is short compared to the length scale for changes in the pressure. In the hydrodynamic approximation, the motions of plasma atoms and molecules obey Maxwellian statistics and the plasma behavior can be described in terms of macroscopic observables. There are situations when the plasma motion is not hydrodynamic, such as when the vapor in a low density target chamber like HIBALL (Böhne 1982) is near the end of its recondensation phase, but in these cases the invalidity of the hydrodynamic approximation does not lead to unexpected results.

Within the hydrodynamics approximation the plasma motion is calculated by simultaneously solving the continuity equation, conservation of momentum, and conservation of energy. These equations can be expressed as follows: continuity,

$$\frac{\partial \rho}{\partial t} + \vec{\nabla} \cdot \rho \vec{u} = 0 \ , \tag{25}$$

where u is the fluid velocity; momentum,

$$\rho \left(\frac{\partial \vec{u}}{\partial t} + \vec{u} \cdot \vec{\nabla} \vec{u} \right) = -\vec{\nabla} P \ , \tag{26}$$

where P is the plasma pressure; and energy

$$\frac{\partial}{\partial t} \left(\rho \varepsilon + \frac{\rho u^2}{2} \right) = -\vec{\nabla} \cdot \left[\rho \vec{u} \left(\varepsilon + \frac{u^2}{2} \right) + P \vec{u} \right] + \rho Q \ , \tag{27}$$

where ε is the plasma specific energy density and Q is the net specific energy sources and sinks. The plasma pressure and energy density are related to the temperature and density of the plasma through the equation of state. In addition to external sources, Q includes the effects of thermal conduction and radiative transfer, which is discussed in Section 4.4.

Thermal conduction includes local effects, such as thermal diffusion, and nonlocal effects, such as long range transport of locally produced electrons or ions. Nonlocal effects are probably not important in target chambers because the plasma does not produce populations of energetic charged particles. Thermal conduction is important and includes both classical thermal diffusion and turbulent effects (Gilligan 1989). The first term of equation 27 due to thermal diffusion is

$$\rho Q_{thermal} = -\vec{\nabla} \cdot \vec{q} = -\vec{\nabla} \cdot (-\kappa \vec{\nabla} T) \; . \tag{28}$$

Here, $\vec{q}$ is the thermal conduction flux and κ is the thermal conductivity. The Spitzer thermal conductivity (Spitzer 1962) is often used for target chamber plasmas. One needs to use tabulated values for neutral gases. The easiest way to include turbulent heat transfer is to use tabulated values for neutral gases. The easiest way to include turbulent heat transfer in equation 28 is to modify κ. This requires a priori knowledge of the plasma conditions. In principle, one could calculate the modified κ, based on plasma conditions.

The numeric solution of the hydrodynamic equations is most often done within a Lagrangian spatial finite differencing scheme. With this method, hydrodynamic zones are defined within the plasma. The boundaries of these zones move with the local fluid velocity. There are two major advantages to Lagrangian differencing: zones automatically follow shock fronts, and the nonlinear convection terms in the hydrodynamic equations are replaced by a single time differencing expression, making the solution faster. The bulk fluid kinetic energy terms in the energy equation are also removed from the energy equation. For accuracy, adjacent zones must have approximately equal masses. This is a difficult task in multidimensional codes and can lead to a very large number of zones even in one dimension

when modeling solid-plasma interfaces. With Lagrangian differencing and with modifications to Q and the thermal conduction term, the one-dimensional version of equation 27 becomes

$$\frac{\partial \varepsilon}{\partial t} = \frac{\partial}{\partial m_o}\left(r^{\delta-1}\kappa\frac{\partial T}{\partial r}\right) - \frac{\partial(1/\rho)}{\partial t}\left(P + \left[\frac{\partial \varepsilon}{\partial(1/\rho)}\right]_T + q_{visc}\right) + S_{abs} - J + S\ . \qquad (29)$$

Here, m_o is the mass in Lagrangian zones, S_{abs} is the rate at which energy is absorbed from radiation, J is radiation emission, and q_{visc} is the artificial viscosity. The artificial viscosity is a pressure–like term that spreads shock discontinuities across several zones (Richtmyer & Morton 1967). Adaptive grid techniques reduce the number of required zones by placing zones only at positions that are needed on each time step, but this method is still under development and is not used in current production computer codes.

These equations have been written assuming that the plasma electrons and ions move together and have the same temperature. If one invokes charge neutrality, then the free electron density is equal to the ion charge density. If the electrons and ions move together, then a single momentum conservation equation can be solved. It is quite possible that the electrons and ions do not have the same temperature. Then it is common to treat the plasma as a single fluid, but with distinct electron and ion temperatures and coupled electron and ion energy conservation equations.

4.3.1. Equations of State

The equations of state are necessary to solving the hydrodynamic equations. The equations of state provide the ionization fraction and the electron and ion pressure and energy density as functions of mass density and temperatures. In some applications, these are calculated within the solution to the hydrodynamics equations, but generally they are pre-calculated for a density–temperature grid and table interpolation is used in the hydrodynamics code. The disadvantage of this approach is that the plasma is assumed to be in an equilibrium, which is only true as long as the properties of the plasma are changing

more slowly than the mean collision time. If one uses this approach there are tables such as SESAME (Bennett 1978) available.

For plasma densities that are orders of magnitude below the solid or liquid density and where the plasma is in local thermodynamic equilibrium (LTE), the charge state can be calculated with the Saha model. For the plasma to be in LTE, the radiation field must be weak enough to not affect the populations of charge states. Under these conditions, one can use Boltzmann statistics to relate the populations of different charge states to each other. This approach (Zel'dovich & Raizer 1966; Mihalas 1978) yields a set of coupled equations:

$$\frac{n_{m+1}n_e}{n_m} = 2\frac{u_{m+1}}{u_m}\left(\frac{2\pi m_e kT}{h^2}\right)^{3/2}\exp\left(-\frac{I_{m+1}}{kT}\right) . \tag{30}$$

Here, n_m is the population of ions with charge state m, which has an ionization potential I_{m+1}. u_m is the electronic partition function

$$u_m = \sum_{k=0}^{k_{max}} g_k \exp\left(-\frac{E_k - E_o}{kT}\right) , \tag{31}$$

where g_k is the number of electrons in shell k and E_k is the energy of that shell. For an LTE plasma, the population of charge states is a function of temperature and density. Here, we have assumed that the electrons and ions have the same temperature.

If the plasma is not in LTE, then quasi-equilibrium models like the Coronal approximation can be used. Otherwise, a fully time-dependent calculation of population densities is required.

However ionization is calculated, the specific energy density is often taken to be an ideal gas with the energies of excitation and ionization included,

$$\varepsilon = \left[1 + \sum_{k=0}^{k_{max}} n_k\left(1 + \frac{2I_k}{3kT}\right)\right]\frac{3kT}{2} . \tag{32}$$

The pressure of such a plasma is

$$P = \left(1 + \sum_{k=0}^{k_{max}} n_k\right) kT \ . \tag{33}$$

Here we have once again assumed that the electrons and ions have the same temperature. If this is not the case, equations 32 and 33 will be slightly modified.

If the plasma or vapor is at or near solid or liquid density, the situation is very different. In ICF target chambers the vapor generated by target emanations is initially high density and low temperature. The equation of state of this vapor is important to the pressure loading on the target chamber wall. As long as the temperature is not high enough to excite electronic and lattice contributions (below about 1 eV), one can use solid or liquid models for the equation of state. The transition from a solid to an ideal gas is difficult to model and is usually done in some numerically smooth manner. At high density, outer atomic electrons are free even at low temperature because of reduction in the effective ionization potential due to interatomic forces. Also, at high density the electrons are degenerate and must obey Fermi-Dirac statistics. We will not discuss detailed behavior of electrons in a solid. In a solid, the motion of ions is restricted to vibrations about lattice sites. Zel'dovich (Zel'dovich & Raizer 1966) gives a good summary of low temperature high density equations of state. High temperature high density equations of state also exist(More 1988), but they are less relevant to ICF target chamber conditions. The essentials of high density low temperature equations of state are that the energy density consists of contributions from the interaction between atoms, ε_c and P_c, from the vibrational motion of the ions, ε_T and P_T, and from the electrons, ε_e and P_e. The ion vibrational contributions are;

$$\varepsilon_T = \frac{3Nk}{\rho}(T - T_o) + \varepsilon_o \ , \tag{34}$$

where ε_o is the thermal energy of the atomic lattice at T_o, room temperature, and

$$P_T = \Gamma \varepsilon_T \rho \ , \tag{35}$$

where Γ is the Grüneisen coefficient.

4.4. Radiative Transfer

Radiative transfer is an important mechanism of heat transfer in ICF target chambers. In gas protected first surface designs, radiation is the primary manner in which energy transports to the first surface. The rate at which energy is radiated to the surface has a great influence on the target chamber design. In sacrificial first surface concepts, the transport of energy within the material vaporized from the surface can be mostly radiative. Methods of calculating radiative transfer can be very computationally expensive, with more spectral detail being more expensive. It is best to choose the least detailed method that adequately models the target chamber conditions.

An example of a target chamber design that is sensitive to the choice of radiative transfer method is SIRIUS. The essential feature of the SIRIUS target chamber designs is the absorption of the target x rays and debris ions in 0.5 to 1.0 torr xenon gas. The plasma reradiates the absorbed energy to the wall. The details of the reradiation must be accurately calculated to properly analyze such a design. The time-integrated flux of photons on the target chamber wall is shown for the SIRIUS-T design in Figure 17. Here, the results of simulations performed with the CONRAD code are shown (Peterson 1992). CONRAD uses a multigroup diffusion method to transport radiation (Peterson 1988) and results are shown for different numbers of photon energy groups. It is clear that the group structure is important. The use of 180 energy groups in this case predicts a slower diffusion of energy to the target chamber wall than do calculations with fewer groups. A calculation has been performed where radiation is transported as atomic lines and where modification of the populations of atomic states among the plasma atoms by the radiation is considered (MacFarlane 1991). It is seen in Figure 18 that the spectrum of radiation on the first wall predicted by a line transport calculation is quite different from the spectrum from a 20 group diffusion calculation.

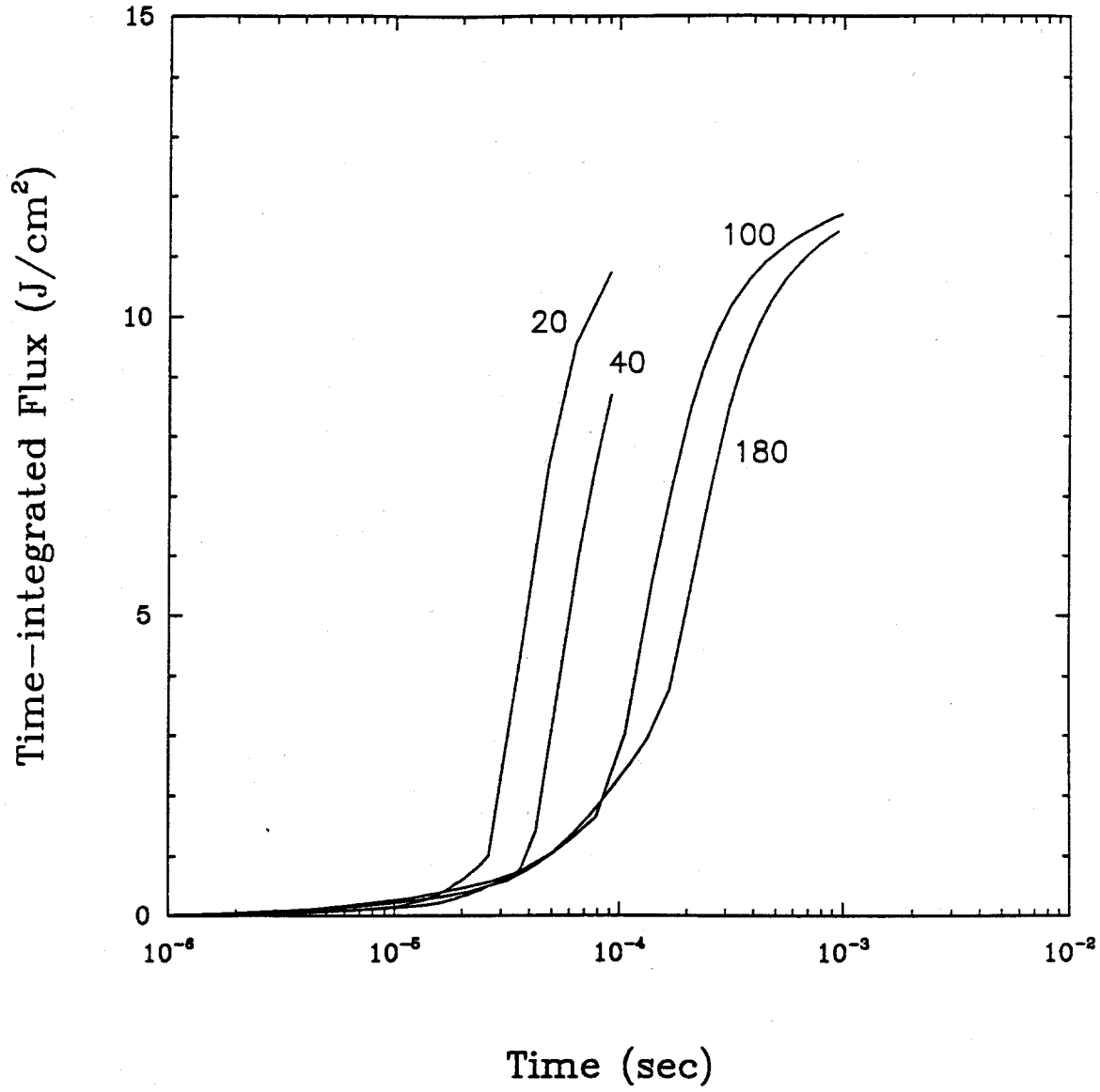

Figure 17. Time-integrated radiation flux on the wall of the SIRIUS-T target chamber. Calculated with a radiation diffusion model using a variety of energy group structures.

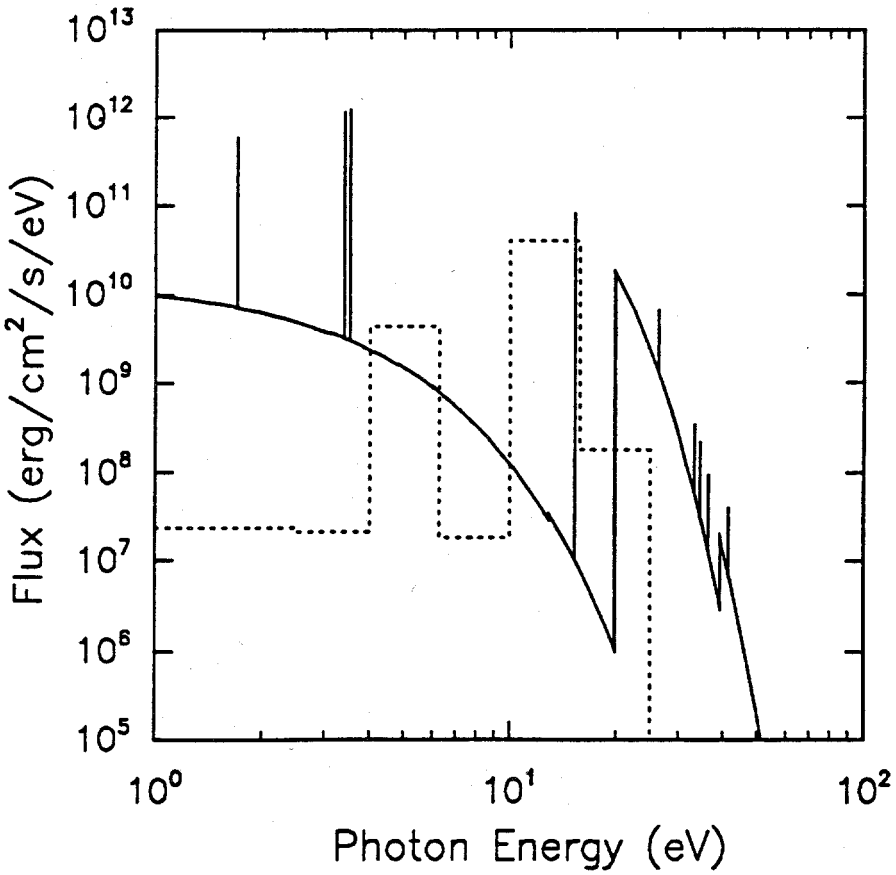

Figure 18. Comparison of the spectral flux on the wall of the SIRIUS-T target chamber. Calculated with a line transport model with modification of the background plasma by the radiation (solid curve) or with a 20 group diffusion calculation (dotted curve).

4.4.1. Radiative Transfer Methods

The most general way to calculate radiative transfer is with the transfer equation:

$$\left[\frac{1}{c}\left(\frac{\partial}{\partial t}\right) + \left(\frac{\partial}{\partial s}\right)\right] I(\vec{x}, t; \vec{n}, \nu) = \eta(\vec{x}, t; \vec{n}, \nu) - \chi(\vec{x}, t; \vec{n}, \nu) I(\vec{x}, t; \vec{n}, \nu) \ . \tag{36}$$

$I(\vec{x}, t; \vec{n}, \nu)$ is the intensity of radiation at position $\vec{x}$, time t, direction $\vec{n}$, and frequency ν. s is the path length the radiation takes through an element of material. η is the rate at which

radiation is created through emission, and χ is the opacity of the material. χ should include the effects of both absorption and radiation scattering. The transfer equation itself is rarely solved, but a variety of approximations to the transfer equation are commonly used. We will discuss multigroup radiation diffusion, the discrete ordinates, and Monte Carlo methods. A number of excellent texts discuss these and other methods in detail (Zel'dovich & Raizer 1966; Mihalas 1978; Mihalas & Mihalas 1984). These methods are similar in that they assume that the radiation does not significantly alter the atomic structure of the medium. Under target chamber conditions, atomic lines can alter the medium, so we will discuss a method for considering this line trapping effect.

Multigroup Diffusion. The multigroup diffusion method is used in many of today's radiation-hydrodynamics computer codes. The photon spectrum is divided into a finite number of frequency groups, where η and χ are averaged in some way across each group. The diffusion method requires that the radiation is approximately isotropic (linearly anisotropic). This condition is met when the photon mean free paths are small compared to the length scales for changes in the temperature or density of the medium. Under these conditions, called the diffusion limit, the transfer equation reduces to the radiation diffusion equation:

$$\frac{1}{c}\frac{\partial E_\nu}{\partial t} = \frac{1}{3}\vec{\nabla}\cdot\left(\frac{1}{\chi_\nu}\vec{\nabla}E_\nu\right) + \left(\frac{4\pi}{c}\right)\eta_\nu - \chi_\nu E_\nu \ . \tag{37}$$

E_ν is the radiation energy density for the photon energy group centered around energy hν. χ_ν and η_ν are the group averaged opacity and emission for that group. The specific dependence on time and position have been omitted for the sake of brevity. The dependence on direction has been integrated away.

One-dimensional finite differencing schemes have been developed to solve this set of equations (one equation for each energy group) for Lagrangian, Eulerian and adaptive grid spatial meshing, and for explicit and implicit time differencing. Lagrangian differencing is most common and there are several well developed computer codes that use this scheme. Lagrangian differencing has the disadvantage that the mesh moves with the fluid and does

not necessarily place the most mesh points in positions where the radiation intensity has the largest gradient. With adaptive grids, the mesh can be programmed to be more advantageous to solving the radiation diffusion equations. There are currently no codes commonly used in ICF target chamber analysis that use adaptive grids, though the use of this in radiation-hydrodynamics codes is an active area of research. Implicit differencing leads to more stable codes with larger time steps than do time-centered differencing. In the solution to the radiation diffusion equations, local values of χ_ν and η_ν can change very rapidly in time in ICF target chamber applications, which means that small time steps are often required even for implicit differencing. The advantage of implicit differencing is, therefore, mostly in the stability. Explicit codes often require iterations of each time step to achieve stability, making implicit codes faster.

Nonisotropic Radiative Transfer. In media that are not optically thick, radiation cannot be considered approximately isotropic. The radiation diffusion method is not valid under such conditions. The direction of the radiation, $\vec{n}$ in equation 36, must be explicitly treated. Three approaches to radiative transfer in non-optically thick media that are well developed are flux limited diffusion, discrete ordinates, and Monte Carlo.

Flux limited diffusion uses the same general formalism as radiation diffusion, but it modifies the effective diffusion coefficient in equation 37 so that when the medium is optically thin, radiation propagates at the speed of light. Without this adjustment equation 37 has an infinite propagation speed as χ_ν approaches zero. This method is correct in the diffusion limit and in the limit of $\chi_\nu = 0$ and is numerically stable, but it is not necessarily correct for marginally thin media.

The discrete ordinates and Monte Carlo methods are useful for modeling radiative transfer in marginally thin media. The discrete ordinates method approximates the radiation intensity as a collection of rays, each moving in a different direction. The directions are defined by μ_i, direction cosines between $\vec{n}$ and reference directions. The $2M$ values of μ_i and

quadrature weights, b_i are chosen such that:

$$\int_{-1}^{1} I_{nu}(\mu)d\mu = \sum_{i=-M}^{M} b_i I_{nu,i}. \tag{38}$$

The Monte Carlo method generates an ensemble of photons with random directions and calculates their trajectories in the medium. The discrete ordinates method often is not useful in optically thick media and requires a large value for M in optically thin target chambers. The Monte Carlo method requires an ensemble of many photons to obtain reasonable accuracy, but it is particularly well suited to complex multidimensional geometries.

Line Transport. In plasmas that have optical depths less than unity, atomic lines are an important part of the photon spectrum. In plasmas that are optically thick to the lines, yet are optically thin to the continuum, the transport of lines is especially important. In line transport, the radiant energy is confined to very narrow parts of the spectrum. The lines essentially only interact by reversing the process that created them in different atoms. Therefore, they only interact with atoms in a given atomic excited state (the final state in the bound-bound transition that created the photon). There is only a fraction of the atoms in that state in the absorbing plasma. Therefore, a great many photons may be interacting with a small number of atoms, a situation perfect for radiation modifying the populations of plasma atom excited states.

One needs a model that includes the effects of photoexcitation and photoionization on the atomic level populations. The population of each atomic level is determined by collisional and radiative coupling between levels. The rate equation for level i can be written as,

$$\frac{dn_i}{dt} = -n_i \sum_{j\neq i}^{N_L} W_{ij} + \sum_{j\neq i}^{N_L} n_j W_{ji} \ , \tag{39}$$

where $W_{i,j}$ is the transition rate for state i to j, n_i is the population of level i, and N_L is the total number of levels in the system. The upward transition rates ($i < j$) are expressed as,

$$W_{i,j} = B_{ij}\bar{J}_{ij} + n_e C_{ij} + n_e \gamma_{ij} + R_{i,j} \ , \tag{40}$$

and the downward rates ($i > j$) are,

$$W_{i,j} = A_{ij} + B'_{ij}\bar{J}_{ij} + n_e D_{ij} + n_e \alpha_{ij} + R'_{i,j} + n_e^2 \delta_{ij} \ . \tag{41}$$

n_e is the electron density and $\bar{J}_{ij} = \int \phi_{ij}(\nu) J_\nu d\nu$, where $\phi_{ij}(\nu)$ is the line profile for transition i to j. The coefficients in these two equations are spontaneous emission (A_{ij}), stimulated absorption (B_{ij}) and emission (B'_{ij}), collision excitation (C_{ij}), and deexcitation (D_{ij}), radiative plus dielectronic recombination (α_{ij}), collisional ionization (γ_{ij}), collisional recombination (δ_{ij}), photoabsorption (R_{ij}), and stimulated recombinations (R'_{ij}). Equation 39 is often solved in a steady state approximation (MacFarlane & Wang 1991) by setting $dn_i/dt = 0$. This system of equations is coupled to a solution to the radiative transfer equation to find J_ν. One approach is an escape probability method (Apruzese 1984) to calculate J_ν.

4.4.2. Opacity Models

The opacity of plasmas and vapors in ICF target chambers can greatly influence target chamber performance. Opacity is due to the absorption of photons through bound-bound, bound-free, and free-free atomic processes. In our discussion here, each absorption process is related to its inverse emission process through the principle of detailed balance (Zel'dovich & Raizer 1966), which is only valid when the medium is in LTE (or quasi-LTE). Under these conditions, only the absorption opacity needs to be provided, and emission can be easily calculated from it. The cross sections given below are generally in the non-relativistic limit, implying that the electron kinetic energies are well below the electron rest energy. This is valid for most ICF target chamber situations, the most important exception being inner shell line radiation from high atomic number elements.

The cross section for the absorption of a photon through a bound electron to bound electron transition in an atom is,

$$\sigma_{bb\nu nn'} = \frac{e^2}{m_e c}\frac{\Gamma_{nn'}}{4\pi} f_{nn'} \frac{1}{(\nu - \nu_{nn'})^2 + (\Gamma_{nn'}/4\pi)^2} \ , \tag{42}$$

for a transition from state n to n' and a photon energy $h\nu$. $\Gamma_{nn'}$ is the line width and $f_{nn'}$ is the oscillator strength of that transition. $f_{nn'}$ is measured for a small fraction of transitions (Smith & Weise 1971), but it must usually be calculated quantum mechanically (Wang 1992). The line width is greatly influenced by the plasma the absorbing atom finds itself in, as the fields from neighboring atoms increase the line width (Griem 1974).

The cross section for the absorption of photons through bound-free transitions (photoionization) can be expressed as

$$\sigma_{bf\nu n} = \frac{64\pi^4}{\sqrt{3}} \frac{e^{10} m_e Z^4}{h^6 c \nu^3 n^5} \ . \tag{43}$$

This assumes that the ionizing atom is "hydrogen-like". "Hydrogen-like" atoms are those in which the electron performing the transition is in a large enough orbit that the screened nuclear charge is effectively a point. The electron wave functions will then be similar to those of the hydrogen atom, though the nuclear charge need not be one. The cross section is zero when the photon energy is below the energy required to ionize, $\frac{2\pi^2 m_e e^4 Z^2}{h^2 n^2}$ for "hydrogen-like" atoms. The photoionization is of an atom of remainder nuclear charge (after ionization) Z which loses an electron with principal quantum number n.

Free-free transitions occur when a free electron either emits or absorbs a photon and remains a free electron, though of a new energy. To conserve both energy and momentum, this transition may only occur in the presence of a third body, usually either an ion or a neutral atom. Normally, under ICF target chamber conditions, the electrons are free to have any energy and momentum, though if the free electron gas is dense and cold enough to be degenerate or if free-free transitions in a solid are being considered, electrons may only make transitions to unfilled states. For a nondegenerate electron gas, Born approximation

calculations (Heitler 1944) provide a Bremsstrahlung cross section for an ion with charge state Z of

$$\sigma_{ff\nu} = \frac{16}{3}\frac{Z^2 e^2}{\hbar c}\left(e^2 m_e c^2\right)^2 \left(\frac{c}{v}\right)^2 \frac{1}{\hbar\omega} \ln\left[\frac{\left(\sqrt{E}+\sqrt{E-\hbar\omega}\right)^2}{\hbar\omega}\right] . \tag{44}$$

Here, the cross section is in units of area per unit photon energy. $E = \frac{m_e v^2}{2}$ is the initial energy of the electron. The cross section for a neutral atom is reduced by approximately a factor of $E^2/4I_H^2 Z^2$, where I_H is the ionization energy of a hydrogen atom.

When using a multigroup diffusion method for radiation transport, one must average the opacity across the width of the group. This is relatively easy for free-free and bound-free contributions to the opacity because, if one avoids placing the major bound-free edges in the middle of an energy group, the cross sections are smoothly varying across reasonably broad groups. The situation is reversed for bound-bound lines, when the line widths are hopelessly narrow in comparison to the group widths. There are two standard methods of performing group averages, Rosseland and Planck. The absorption coefficient is calculated from the cross sections and atomic and electron populations,

$$\begin{aligned}\kappa_\nu &= \sum_Z N_e N_Z \left[1-\exp(-h\nu/kT)\right]\sigma_{ff\nu}(Z) + \\ &\quad \sum_{Z,n=n^*}^{\infty}\left[N_{Zn} - N_{Zn}^{LTE}\exp(-h\nu/kT)\right]\sigma_{bf\nu n}(Z) + \\ &\quad \sum_{Z,n,n'}\left[N_{Zn} - N_{Zn'}\left(\frac{g_{Zn}}{g_{Zn'}}\right)\right]\sigma_{bb\nu nn'}(Z) .\end{aligned} \tag{45}$$

The sums over Z, n, and n' represent charge state and upper and lower atomic levels. The N's represent populations of various species and states, and N_{Zn}^{LTE} is the LTE population of ions with charge state Z and level n after photoionization. g_{Zn} is the number of electrons in a shell. The emission coefficient can be calculated for situations that are not in LTE as

(MacFarlane 1987)

$$\begin{aligned}\eta_\nu &= \sum_Z N_e N_{Z+1} \exp(-h\nu/kT)\sigma_{ff\nu}(Z) + \\ &\sum_{Z,n=n^*}^{\infty} N_{Zn}^{LTE} \exp(-h\nu/kT)\sigma_{bf\nu n}(Z) + \\ &\sum_{Z,n,n'} N_{Zn'} \left(\frac{g_{Zn}}{g_{Zn'}}\right) \sigma_{bb\nu nn'}(Z) \ . \end{aligned} \tag{46}$$

The Planck opacity is used in calculating the radiation emission in multigroup radiation diffusion calculations. The Planck opacity for energy group g is

$$\sigma_{P,g} = \frac{1}{\rho} \frac{\int_{\nu_g}^{\nu_{g+1}} \eta_\nu d\nu}{\int_{\nu_g}^{\nu_{g+1}} B_\nu(T) d\nu} \ , \tag{47}$$

where $B_\nu(T)$ is the Planck function at temperature T and frequency ν. The Planck opacity adds in the lines with the other contributions. The Rosseland opacity is used in the transport of radiation in the diffusion method. The Rosseland opacity for energy group g is

$$\sigma_{R,g} = \frac{1}{\rho} \frac{\int_{\nu_g}^{\nu_{g+1}} \left(\frac{\partial B_\nu}{\partial T}\right) d\nu}{\int_{\nu_g}^{\nu_{g+1}} \left(\frac{\partial B_\nu}{\partial T}\right) \frac{1}{\kappa_\nu + s_{nu}} d\nu} \ , \tag{48}$$

where s_ν is a term to account for photon scattering. The Rosseland opacity more heavily weights the low absorption coefficient parts of the spectrum. The effect is to reduce the effect of lines. This is the correct approach in the diffusion limit as the lines diffuse much more slowly than the continuum. In marginally thick plasmas, which are thin to the continuum and thick to the lines, the Rosseland opacity will perform very badly because the behavior of the lines is important.

4.5. Computer Codes

4.5.1. One-Dimensional Lagrangian Hydrodynamics

A number of one-dimensional Lagrangian computer codes can be used to simulate target chamber phenomena. We will discuss the CONRAD computer code, which has been developed at the University of Wisconsin specifically to study ICF target chamber phenomena. The KATACO code (Goel 1992) under development at Kernforschungszentrum Karlsruhe is based on the MEDUSA code (Christiansen 1974). It is similar to CONRAD is many ways and will not be discussed here.

CONRAD. CONRAD is a one-dimensional Lagrangian radiation hydrodynamics computer code (Peterson 1988). CONRAD has been under development at the University of Wisconsin-Madison for the past 15 years. Examples of the past and current uses of CONRAD include modeling of blast effects in ICF target chamber designs, laser ablation driven shock experiments in gases, x-ray driven shocks in solids, and vaporization of material on tokamak divertors during disruptions. Using the code to simulate these different phenomena has led to verification of the code under a range of conditions.

CONRAD can be run in spherical, slab, or cylindrical geometry. The user can specify each Lagrangian zone boundary at the start of each run or can use an automatic zoning option. CONRAD has a limited rezoning ability to change the zoning in the middle of a run. The hydrodynamic motion is calculated with explicit time differencing. Material is accelerated by the combined plasma and radiation pressure and artificial viscosity pseudo-pressure. Reflecting hydrodynamic boundary conditions are imposed at both ends of the Lagrangian mesh. Numerically, CONRAD solves an explicitly time differenced version of equation 26 to find the velocity in each zone, and then calculates the positions of zone boundaries.

Energy transport in CONRAD includes thermal conduction and multigroup flux-limited radiation diffusion. Radiation absorption and emission terms couple the radiation to

the thermal energy. The thermal energy equation solved in CONRAD is:

$$C_v \frac{\partial T}{\partial t} = \frac{\partial}{\partial m_o}\left(r^{\delta-1}\kappa_p \frac{\partial T}{\partial r}\right) - P_p \dot{V} - \left(\frac{\partial (C_v T)}{\partial V}\right)_T \dot{V} - q\dot{V} + A - J + S \; . \tag{49}$$

Here, $V = 1/\rho$, κ_p is the Spitzer plasma conductivity, m_o is Lagrangian mass, and δ is the geometry parameter (= 1, slab; 2, cylindrical; and 3, spherical). The radiation diffusion equation for frequency group g is:

$$V \frac{\partial E_R^g}{\partial t} = \frac{\partial}{\partial m_o}\left(r^{\delta-1}\kappa_R^g \frac{\partial E_R^g}{\partial r}\right) - \frac{4}{3} E_R^g \dot{V} - c\sigma_P^g E_R^g + J^g \; g = 1, ..., G \; . \tag{50}$$

Here, E_R^g is the radiant energy in a zone in group g. $\kappa_R^g = \frac{cV}{3\sigma_R^g}$ is the radiation conductivity, and J^g is the radiation emitted into group g. $A = \sum_g cE_R^g$ and $J = \sum_g J_g$ are the absorption and emission terms. S is an energy source to the plasma, and includes ion and x-ray deposition from ICF targets. When the radiation equation is differenced, a flux limiter is included that smoothly limits the radiation flux in each group to the speed of light times the radiation energy density. In this multigroup method, CONRAD solves these equations fully implicitly. CONRAD has been written so that these equations are solved in a highly vectorized manner, when the code is running on a Cray supercomputer. There is a single radiation group option in CONRAD that solves these equations implicitly, but the multigroup option is most often used. CONRAD performs an energy conservation check at the conclusion of every time cycle. With proper zoning and time step constraints, CONRAD can achieve about 95% energy conservation for ICF target chamber problems.

The source term, S, in equation 49 includes x ray and ion deposition. CONRAD does no electron deposition. Both x rays and ions enter the Lagrangian mesh through the lower zone boundary of zone number 1. Both x rays and ions are travelling in the direction toward larger zone indicies. Ion deposition is calculated using the physics models discussed in section 4.1.1. CONRAD allows the user to choose to have the in-flight ion charge

calculated (considering charge exchange) by CONRAD or to use a constant ion charge. It has been found that allowing CONRAD to calculate the in-flight ion charge gives results that are in better agreement with experiment. Each time step, a number of packets of ions is created, each with a given ion species and ion energy. The ions, starting at the edge of first zone, travel toward larger zone index at the calculated speed. Each time step, the position and energy are updated by calculating dE/dx and the new ion speed. Each ion in the packet loses energy at the same rate, until the packet either reaches the other end of the mesh and leaves the hydrodynamic mesh, or the packet loses all of its energy through deposition. X-ray deposition is calculated by using the empirical formulae for cold x ray stopping powers compiled by Biggs and Lighthill (1988). The x rays are intense enough in ICF target chambers that the populations of electrons can become depleted in the atomic shells that are responsible for the absorption of x rays. This leads to a reduction in the x ray stopping power. CONRAD treats this bleaching effect by reducing the stopping power (McCarville 1981). The x-ray source is treated as usual photons, but is assumed to travel at infinite speed and is deposited where the stopping power dictates in the same time step that it is introduced in the first zone. The user can specify a time and energy dependent source.

CONRAD calculates energy deposition, heat transfer, and vaporization in material that is in contact with the high index edge of the Lagrangian hydrodynamic mesh. The material is zoned into Lagrangian hydrodynamic zones. A zone is not allowed to move until it is declared to be vaporized, at which point it becomes part of the Lagrangian hydrodynamic calculation, which was discussed earlier in this section. As long as a zone is considered to be not vaporized, energy from ions, radiation, thermal conduction, and latent heat from recondensation of vapor are deposited in the unvaporized zone nearest the hydrodynamic mesh. X-ray energy is deposited in a profile calculated in the same way as x-ray deposition in the gas hydrodynamic zones. Thermal conduction in the unvaporized mesh is calculated with a standard temperature diffusion method. CONRAD uses either of the vaporization methods

discussed in section 4.2.1 to determine if a zone is vaporized or not. Careful accounting of the latent heat is done. Condensation is done as dicussed in section 4.2.3. CONRAD does not currently consider melting.

4.5.2. Other Hydrodynamics

One-dimensional Lagrangian hydrodynamics computer codes are not useful for all ICF target chamber conditions. Often, two-dimensional effects are important. Two-dimensional Lagrangian codes do exist but are not generally available and can be difficult to use. Multidimensional Eulerian codes are available and easier to use, though they do not have the advantages of Lagrangian hydrodynamics discussed earlier. The CSQ code has mixed Eulerian–Lagrangian hydrodynamics and has been used for ICF target chamber simulations.

CSQ III. CSQ III is a two dimensional finite difference hydrodynamics code with elaborate equation of state capabilities (Thompson 1988). It uses a Lagrangian update of the fluid motion with continuous rezoning to construct Eulerian differencing. It includes material strength phenomena, radiative transfer, thermal conduction, fracturing, high explosives phenomena, porosity phenomena, and a variety of boundary conditions. CSQ is particularly useful for simulations of shocks in solids. The modeling of detailed phenonema in solid material distinguishes CSQ from a code like CONRAD. The launching of shocks in the solid structures in an ICF target chamber by x-ray driven vaporization is an important issue, which CSQ can be used to study. CSQ is not particularly suited for target chamber gas phenomena since it only does single frequency group radiation diffusion, which is sufficient for modelling shocks in solids, but not for fireball dynamics.

Radiation Transport Alone. Detailed radiation transport including lines can be most easily considered when decoupled from the hydrodynamic motion. Line transport calculations are performed in a steady state approximation. The chamber gas temperature and density profiles are calculated with a hydrodynamics computer code, and then the radiation transport is calculated for the plasma properties that exist at some point in

time. RATION (Lee 1990) is such a steady state line transport code developed at Lawrence Livermore National Laboratory, which includes hydrogen-like, helium-like and lithium-like atomic lines. Other codes under development at the University of Wisconsin include a more general atomic physics data base that can be used to consider a broader set of lines (MacFarlane 1991).

5. New Developments in Target Chamber Phenomena Modeling

5.1. Radiation-hydrodynamics

Much of the phenomena in gas filled and liquid protected target chambers involves high-temperature hydrodynamic flow. In conventional Lagrangian hydrodynamics the mesh moves at the local fluid velocity and is adapted using the mass density gradient of the fluid. One improvement in radiation-hydrodynamic modeling involves using explicit adaptive mesh algorithms to move the mesh in a consistent way with all fluid and radiation field equations (Yasar 1992). In generalized adaptive algorithms the mesh can move at any velocity and be adapted using any combination of field variables and their gradients. This is useful in tracking gradients that do not correspond to mass density gradients, such as radiation diffusion fronts. Such codes are in early stages of testing on problems of interest to reactor chambers (Yasar 1991).

One and two dimensional models of gas dynamics using a second order Godunov method have been used to study ablated material motion and shock propagation in liquid protected reactor chambers (Chen 1992a). This model is particularly good for following shocks since it does not suffer from the numerical diffusion that Lagrangian codes do. There is no treatment of radiation in this model yet and the Eulerian mesh demands that a remesh be done to follow the flow of the ablated material to the center of the chamber. The same Godunov method has been used in the TSUNAMI code to study the flow of vapor through the array of liquid jets in the HYLIFE design (Liu 1992). This model strictly solves the Euler

equations but future developments include introducing radiative transfer, condensation, and a non-ideal equation of state.

Radiative emission to plasma-facing surfaces is the key to gas filled target chamber design. Recent analysis has shown that conventional multigroup methods of radiative transfer are inadequate to model this phenomena because the plasma is not in thermodynamic equilibrium and because the plasma is optically thick to line radiation and optically thin to the continuum. The use of spectrum averaged Planck and Rosseland multifrequency opacities greatly overestimates the plasma emission in many circumstances of interest. A great amount of work has recently been done in the astrophysical community in collisional-radiative-equilibrium (CRE) modeling of plasmas and escape probability modeling of line radiation and this has been adapted to target chamber plasmas (MacFarlane 1991). Detailed accounting of the most important lines in the most important ionization and excitation states is done. The level populations are computed self-consistently with the line radiation field so that the important effects of photoionization and photoexcitation are included in determining the level populations. This is shown schematically in Figure 19 for a simple three level atom. Detailed calculations quickly create a very large computational burden because level populations (N_L) are computed for each spatial zone (N_Z) and these quantities are coupled by the radiation field. Escape probabilities can be computed using line profile averages and chord length averages across the plasma or can themselves be computed using more accurate multifrequency and multi-angular treatments. The following so-called lambda-iteration procedure is often used for the self-consistent calculation.

1. Make initial guess for population levels.

2. Compute coupling coefficients for transitions of interest.

3. Compute coefficients for grand [(N_L x N_Z) x (N_L x N_Z)] matrix.

4. Solve grand matrix for level populations.

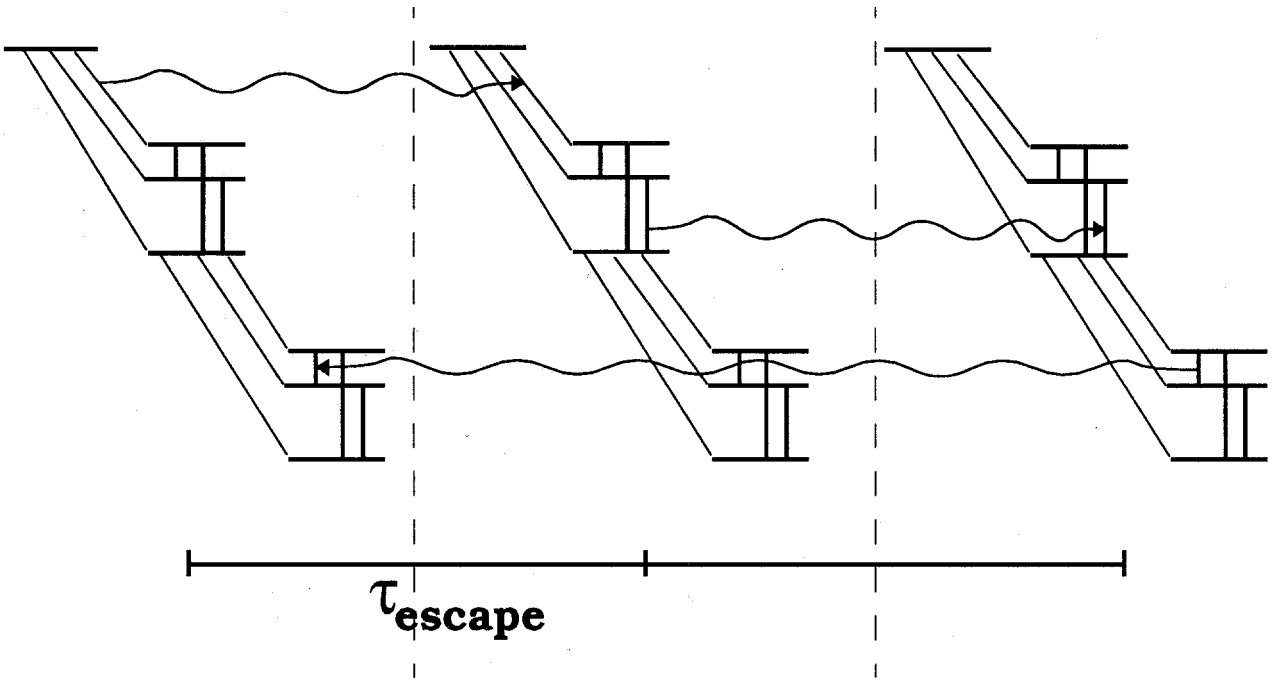

Figure 19. Schematic picture of a three level atom undergoing photoionization and photoexcitation.

5. If new populations are inconsistent with those used to compute coupling coefficients, go to step 2, otherwise calculation is done.

Methods to accelerate this procedure for other applications have been proposed (Apruzese 1984) and there is much more work to be done here for target chamber plasmas. This model is currently used to obtain snapshots in time. Coupling of this radiative transfer model into a time dependent hydrodynamics code has begun. It is expected that the resultant code will be a "Grand Challenge" level computational tool and will require a significant development of parallel computational methods before it is practical for applications.

5.2. Code Verification

The phenomena present in ICF target chambers cannot be duplicated in present experimental facilities. Yet, the computer codes used to study target chamber phenomena must be verified for target chamber relevant conditions. There are a number of experiments that have been or could be performed to simulate some aspects of the target chamber environment. We have identified several areas where verification is possible: target/gas coupling, vaporization, condensation, and radiation transport.

5.2.1. Target/Gas Coupling

The coupling of target energy into the target chamber gases and structures initiates all other target chamber phenomena. Experiments have been performed at the Naval Research Laboratory where a high power laser creates a plume of vapor that drives a shock in a background gas (Ripin 1986). Critical to this, is the deposition of plume ion energy into the background gas. Computer simulations have been performed of these experiments that have shown good agreement once proper attention is paid to the ion deposition physics (MacFarlane 1989).

5.2.2. Vaporization

X-ray driven vaporization in ICF target chambers is critical to sacrificial plasma-facing surfaces designs. Considerable effort has gone into the CONRAD and KATACO codes to simulate this. X-ray driven vaporization occurs over the target x-ray pulse width, which is typically a few ns. Any experiment that simulates x-ray vaporization and resulting pressure loadings on structures needs to have a similar x-ray spectrum, pulse width, and energy fluence. Gas pinches have been able to provide relevant spectra and fluences for a number of years (Spielman 1989), but at a pulse width approximately an order of magnitude too high. Recent advances (Spielman 1992) have reduced gas pinch x-ray pulse widths to a few ns. Some preliminary experiments have been performed with the longer pulse widths (Moses 1991) and some simulations with the CONRAD code are in progess to verify the vaporization method in that code. Futher experiments are needed at the proper pulse widths.

5.2.3. Condensation

Condensation of vaporized material is one of the most difficult phenomena to calculate and is very important to some ICF fusion reactor concepts. Two aspects of condensation that need experimental verification are surface condensation in the presence of noncondensable gases and nucleate condensation. In surface condensation, a volume of vapor would be created by some means that would keep its local temperature above the vaporization temperature. This will prevent nucleate condensation so surface condensation can be studied alone. Nucleate condensation can be studied in a vapor that is cooled below the vaporization temperature. One way to do this is in an expanding vapor such as a vaporizing wire experiment (Bang 1991).

5.2.4. Radiative Transfer

Radiative transfer in target chamber plasmas is a critical issue in many reactor concepts. Experiments are required to verify the opacity models used and the transport

methods. Experiments should create plasmas at relevant densities and temperatures and to measure the time-dependent spectrum at the edge of the plasma. High power lasers or large pulsed power machines are both capable of supplying a large amount of energy quickly enough to perform relevant experiments. Diagnostics of the plasma density and temperature profiles would be required.

Acknowledgment

Support for this work has been provided by Lawrence Livermore National Laboratory, Sandia National Laboratory, and the Kernforschungszentrum Karlsruhe.

REFERENCES

ANDERSEN, H. H. & ZIEGLER, J. F. 1977 *Hydrogen-Stopping Powers and Ranges in All Elements* (Pergamon, New York).

APRUZESE, J. *et al.* 1984 *Phys. Rev. A* **29**, 246.

BAI, R. Y. & SCHROCK, V. E. 1991 *Fusion Tech.* **19**, 732.

BANG, K. H. *et al.* 1991 *Fusion Tech.* **19**, 716.

BARTEL, T. J. *et al.* 1986 *Fusion Tech.* **10**, 1253.

BENNETT, B. I. *et al.* 1978 Los Alamos National Laboratory Report LA–7130.

BIGGS, F. & LIGHTHILL, R. 1988 Sandia National Laboratories Report SAND87–0070.

BLINK, J. A. & Hoover, William C. 1985 *Fusion Tech.* **8**, 1844.

BLINK, J. A 1985a Lawrence Livermore National Laboratory Report UCRL–53604.

BÖHNE, D. *et al.* 1982 *Nucl. Engr. and Design* **73**, 195.

BOURQUE, R. F. *et al.* 1992 *Fusion Tech.* **21**, 1465.

BROWN, M. D. & MOAK, C. D. 1972 *Phys. Rev. B* **6**, 90.

CHEN, X. M. & SCHROCK, V. E. 1991 *Fusion Tech.* **19**, 721.

CHEN, X. M. & SCHROCK, V. E. 1991 *Fusion Tech.* **19**, 727.

CHEN, X. M. *et al.* 1992 *Fusion Tech.* **21**, 1520.

CHEN, X. M. *et al.* 1992 *Fusion Tech.* **21**, 1531.

CHRISTIANSEN, J. P. *et al.* 1974 *Comp. Phys. Comm.* **7** 271.

CRANDALL, D. H. 1992 *Fusion Tech.* **21**, 1451.

ENGELSTAD, R. L. & LOVELL, E. G. 1985 *Fusion Tech.* **8**, 1184.

GILLIGAN, J. *et al.* 1989 *Fusion Tech.* **15**, 522.

GOEL, B. *et al.* 1992 to be published.

GRADY, D. E. 1982 *J. Appl. Phys.* **53**, 322.

GRIEM, H. R. 1974 *Spectral Line Broadening by Plasmas* (Academic, New York).

HEITLER, W. 1944 *The Quantum Theory of Radiation* (Oxford, New York).

HOGAN, W.J. *et al.* 1992 *Physics Today* **45** (9), 42.

JACKSON, J. D. 1962 *Classical Electrodynamics* (Wiley, New York).

KITAGAWA, Y. *et al.* 1992 *Fusion Tech.* **21**, 1460.

KOFFMAN, L. D. *et al.* 1983 *Phys. Fluids* **27**, 876.

LABUNTSOV, D. A. & KRYUKOV, A. P. 1979 *Int. J. Heat Mass Transfer* **22**, 989.

LEE, R. W. 1990 *User Manual for RATION* (Lawrence Livermore National Laboratory).

LIU, J. C. *et al.* 1992 *Fusion Tech.* **21**, 1514.

MacFARLANE, J. J. 1987 University of Wisconsin Fusion Technology Institute Report UWFDM-750.

MacFARLANE, J. J. *et al.* 1989 *Phys. Fluids B* **1** 635.

MacFARLANE, J. J. *et al.* 1990 *Proc. of the 13th IEEE Symp. on Fusion Engineering, October 1989, Knoxville, TN*, 746.

MacFARLANE, J. J. *et al.* 1991 *Fusion Tech.* **19**, 703.

MacFARLANE, J. J. & WANG, P. 1991 *Phys. Fluids B* **3**, 3494.

McCARVILLE, T. J. *et al.* 1981 University of Wisconsin Fusion Technology Institute Report UWFDM–406.

MEHLHORN, T. A. 1981 *J. Appl. Phys.* **52**, 6522.

MEHLHORN, T. A. *et al.* 1983 Sandia National Laboratories Report SAND83 – 1519.

MEIER, W. R. *et al.* 1992 *Proc. of the 14th IEEE/NPSS Symp. on Fusion Engineering, October, 1991, San Diego, CA*, 631.

MIHALAS, D. 1978 *Stellar Atmospheres* (W.H. Freeman, San Francisco).

MIHALAS, D. & MIHALAS, B. W. 1984 *Foundations of Radiation Hydrodynamics* (Oxford, New York).

MILLER, R. B. 1982 *An Introduction to the Physics of Intense Charged Particle Beams* (Plenum, New York) (1982).

MOHANTI, R. B. & GILLIGAN, J. G. 1990 *J. Appl. Phys.* **68**, 5044.

MOIR, R. W. 1991 *Fusion Tech.* **19**, 617.

MOIR, R. W. *et al.* 1992 *Fusion Tech.* **21**, 1492.

MOIR, R. W. 1992a *Fusion Tech.* **21**, 1495.

MONSLER, M. *et al.* 1981 Lawrence Livermore National Laboratory Report UCRL-50021-80, p.9-4.

MORE, R. M. *et al.* 1988 *Phys. Fluids* **31**, 3059.

MOSES, G. & MAGELSSEN, G. 1977 University of Wisconsin Fusion Technology Institute Report UWFDM-194.

MOSES, G. A. & PETERSON, R. 1980 *Nucl. Fusion* **20**, 849.

MOSES, G. A. *et al.* 1985 *Comp. Phys. Comm.* **36**, 249.

MOSES, G. A. *et al.* 1991 *Phys. Fluids* **3**, 2324.

OLSON, R. E. *et al.* 1988 *Proc. of the 12th Symp. on Fusion Engineering, October 1987, Monterey, CA*, 1005.

ORTH, C. D. 1986 *Fusion Tech.* **10**, 1245.

ORTH, C. D. 1990 *Proc. of the 13th IEEE Symp. on Fusion Engineering, October 1989, Knoxville, TN*, 743.

PETERSON, R. R. 1986 *Fusion Tech.* **10**, 1251.

PETERSON, R. R. *et al.* 1988 University of Wisconsin Fusion Technology Institute Report UWDFM-670.

PETERSON, R. R. 1990 *Proc. of the 13th IEEE Symp. on Fusion Engineering, October 1989, Knoxville, TN*, 754.

PETERSON, R. R. *et al.* 1991 University of Wisconsin Fusion Technology Institute Report UWDFM-854.

PETERSON, R. R. *et al.* 1992 *Proc. of the 14th IEEE/NPSS Symp. on Fusion Engineering, October, 1991, San Diego, CA*, 400.

PETERSON, R. R. *et al.* 1992 *Proc. of the 14th IEEE/NPSS Symp. on Fusion Engineering, October, 1991, San Diego, CA*, 1050.

PITTS, J. H. 1990 UCRL-LR 104546, Lawrence Livermore National Laboratory.

PITTS, J. H. & Tabak, Max 1991 *Fusion Tech.* **19**, 640.

PONG, L. *et al.* 1985 *Nucl. Engr. and Design/Fusion* **3**, 47.

RABEAU, M. *et al.* 1992 *Proc. of the 14th IEEE/NPSS Symp. on Fusion Engineering, October, 1991, San Diego, CA*, 1175.

RAFFRAY, A. R. & HOFFMAN, M. A. 1986 *Fusion Tech.* **10**, 1264.

RICHTMYER, R. D. & MORTON, K. W. 1967 *Difference Methods for Initial-Value Problems* (Interscience New York).

RIPIN, B. H. *et al.* 1986 *Laser Interaction and Related Plasma Phenomena* (Plenum, New York) ed. G. H. Miley & H. Hora.

SMITH, M. W. & WEISE, W. 1971 *Astrophys. J. Suppl.* **23**, 103.

SOGA, T. 1982 *Phys. Fluids* **25**, 1978.

SPIELMAN, R. B. *et al.* 1989 *Proc. of the 2nd Intl. Conf. on Dense Z-Pinches, Laguna Beach, CA* (AIP, New York).

SPIELMAN, R. B. *et al.* 1992 *Bull. APS* **37**, 1578.

SPITZER, L. 1962 *Physics of Fully Ionized Gases* (Interscience, New York).

SVIATOSLAVSKY, I. N. *et al.* 1991 *Fusion Tech.* **19**, 634.

SVIATOSLAVSKY, I. N. *et al.* 1990 *Proc. of the 13th IEEE Symp. on Fusion Engineering, October 1989, Knoxville, TN*, 1416.

SVIATOSLAVSKY, I. N. *et al.* 1992 *Proc. of the 14th IEEE/NPSS Symp. on Fusion Engineering, October, 1991, San Diego, CA*, 646.

SVIATOSLAVSKY, I. N. *et al.* 1992a *Fusion Tech.* **21**, 1470.

THOMPSON, S. L. & McGLAUN, J. M. 1988 Sandia National Laboratories Report SAND87-2763.

TILLACK, M. S. *et al.* 1992 *Proc. of the 14th IEEE/NPSS Symp. on Fusion Engineering, October, 1991, San Diego, CA*, 223.

TOBIN, M. T. 1991 *Fusion Tech.* **19**, 679.

WAGANER, L. M. 1992 *Proc. of the 14th IEEE/NPSS Symp. on Fusion Engineering, October, 1991, San Diego, CA*, 636.

WANG, P. *et al.* 1992 submitted to *Phys. Rev.*

YASAR, O. & MOSES, G. 1992 *J. Comp. Physics* **100**, 38.

YASAR, O. & MOSES, G. 1991 *Nucl. Fusion* **31**, 273.

ZEL'DOVICH, Ya. B. & RAIZER, Ya. P. 1966 *Physics of Shock Waves and High-Temperature Hydrodynamic Phenomena* (Academic, New York).